2011

On the Retrieval of the Beam Transverse Wind Velocity Using Angles of Arrival from Spatially Separated Light Sources

Shiril Tichkule
University of Massachusetts Amherst

ON THE RETRIEVAL OF THE BEAM TRANSVERSE WIND VELOCITY USING ANGLES OF ARRIVAL FROM SPATIALLY SEPARATED LIGHT SOURCES

A Thesis Presented

by

SHIRIL TICHKULE

Submitted to the Graduate School of the
University of Massachusetts Amherst in partial fulfillment
of the requirements for the degree of

MASTER OF SCIENCE IN ELECTRICAL AND COMPUTER ENGINEERING

September 2011

Electrical and Computer Engineering

ON THE RETRIEVAL OF THE BEAM TRANSVERSE WIND VELOCITY USING ANGLES OF ARRIVAL FROM SPATIALLY SEPARATED LIGHT SOURCES

A Thesis Presented

by

SHIRIL TICHKULE

Approved as to style and content by:

_____

Andreas Muschinski, Chair

_____

Ramakrishna Janaswamy, Member

_____

Dennis Goeckel, Member

_____

Christopher V. Hollot, Department Head
Electrical and Computer Engineering

To my parents, Sangeeta and Anil.

ACKNOWLEDGMENTS

I express my sincere gratitude to my advisor, Prof. Andreas Muschinski, for the guidance and encouragement he provided throughout my thesis, without which this thesis would not have materialized. I am grateful to the committee members, Prof. Ramakrishna Janaswamy and Prof. Dennis Goeckel, for serving on my thesis committee and for their support and invaluable feedback. I would also like to thank my colleagues, Kekai Hu, Thomas Muschinski, Lucas Root and Shanka Wijesundara, who assisted me in the instrumentation setup and data collection. Thanks are also owed to the staff at the Boulder Atmospheric Observatory for their help in making the facility accessible for carrying out measurements.

I extend a heartfelt thank-you to my colleague and friend, Vijay Venkatesh, who, through his knowledge and resourcefulness has been a great source of inspiration and help throughout my graduate studies. Finally, I would like to thank my friends, Anuj Phadke, Aditya Sarawgi, Ameya Phadke, Sandeep Pillai, Shreyas Panse and Sameer Jade for their assistance and moral support throughout my thesis.

ABSTRACT

ON THE RETRIEVAL OF THE BEAM TRANSVERSE WIND VELOCITY USING ANGLES OF ARRIVAL FROM SPATIALLY SEPARATED LIGHT SOURCES

SEPTEMBER 2011

SHIRIL TICHKULE

B.E., UNIVERSITY OF MUMBAI

M.S.E.C.E., UNIVERSITY OF MASSACHUSETTS AMHERST

Directed by: Professor Andreas Muschinski

For optical propagation through the turbulent atmosphere, the angle of arrival (AOA) cross-correlation function obtained from two spatially separated light sources carries information regarding the transverse wind velocity averaged along the propagation path. Two methods for the retrieval of the beam transverse horizontal wind velocity, v_t, based on the estimation of the time delay to the peak and the slope at zero lag of the AOA cross-correlation function, are presented. Data collected over a two week long experimental campaign conducted at the Boulder Atmospheric Observatory (BAO) site near Erie, CO was analyzed. The RMS difference between $10\,\mathrm{s}$ estimates of v_t retrieved optically, and $10\,\mathrm{s}$ averages of the transverse horizontal wind velocity measured by an ultrasonic anemometer, was found to be $14\,\mathrm{cm\,s^{-1}}$ for the time-delay-to-peak method and $20\,\mathrm{cm\,s^{-1}}$ for the slope-at-zero-lag method, for a 2 h period beginning 0345 MDT on 16 June, 2010, during which the transverse horizontal wind velocity varied between $-1\,\mathrm{m\,s^{-1}}$ and $2\,\mathrm{m\,s^{-1}}$.

TABLE OF CONTENTS

LIST OF TABLES

LIST OF FIGURES

CHAPTER 1

INTRODUCTION AND MOTIVATION

When electromagnetic waves travel through the turbulent atmosphere, their propagation is affected by the integrated effect of local features of the atmosphere along the entire path. These local features manifest themselves as variations in the permittivity (optical refractive index) of air, thereby causing perturbations in the amplitude, phase and the angle of arrival (AOA) of electromagnetic waves propagating through them. For a few applications, these effects are not desirable as they deteriorate the throughput of such systems. In fact, correction techniques have been developed and employed to get rid of these effects. For example, some astronomical telescopes employ adaptive optics to correct for the tilt of the wavefront (caused by atmospheric/ionospheric irregularities) across the telescope aperture and obtain better focused images. From a different perspective though, atmosphere-induced perturbations in electromagnetic waves can also be utilized to decipher features of the atmosphere, such as the wind. A majority of such methods make use of spatially separated receivers/sources, which enable the extraction of the wind vector using the cross-correlation function of the perturbed quantities. Techniques that decipher wind speed using perturbations (amplitude and phase) of electromagnetic waves have been documented in the past in both, optical and radio-wave communities.

Mitra (1949) and Briggs *et al.* (1954) reported measurements of ionospheric winds, based on the scintillation drift of radio waves [16][4]. Cohen *et al.* (1967) devised a technique to obtain the speed of the interplanetary solar wind using radio-star scintil-

lations [9]. Doppler radar has been in the forefront for remote wind measurements in the meteorological community and along with techniques such as the Spaced Antenna (SA) radar, has enabled remote measurements of the three dimensional wind vector [2][13]. Despite the extensive use of radars for remote sensing, the last few decades have seen a gradual rise in the use of optical remote sensors, such as lidars and scintillometers. Although not as extensively used as radars, lidars are naturally suited for remote wind measurements. This is due to the fact that the shorter wavelength of the lidar makes it more sensitive to aerosols, which are good targets for wind sensing, as they follow the motion of the air very well (Chapter 6 in [15]). Moreover, the narrow beamwidth of optical sources such as lasers, enables remote measurements to be made with a much finer spatial resolution. Owing to these facts, considerable progress has been made in the field of optical wind sensing starting from the 1970s onwards.

Lawrence *et al.* (1972) reported the successful construction of the first optical wind sensor that made use of the optical scintillation drift pattern across a pair of photo-detectors, to measure the average wind blowing past a laser beam [14]. Clifford *et al.* (1975) extended the above procedure to infer the transverse wind velocity by observing a random scene [8]. The above techniques made use of the amplitude fluctuation (scintillation) pattern to estimate the transverse wind velocity. When the dimensions of the propagation problem under consideration are much larger than the wavelength of light, the theory of geometrical optics becomes applicable, which is analytically much easier to deal with as diffraction effects can be completely ignored [17]. Hence, the theory of geometrical optics which very well describes the angle of arrival (AOA) fluctuations, can be used to develop an alternative method for remote wind measurements. Cheon *et al.* (2007) derived a technique to estimate the beam transverse (to the optical propagation path) wind velocity, based on the knee frequency observed in the AOA power spectrum of a single light source observed with

2

a telescope [5]. Unfortunately, the use of a single light source caused their wind estimates to lack directional information.

To circumvent the above limitation, a new method that makes the use of a pair of spatially separated light sources to estimate the beam transverse wind velocity is presented in this thesis. The experimental setup used for testing this hypothesis was similar to that used by Cheon *et al.* (with the exception of the use of LEDs instead of flashlight bulbs), but AOA data from a pair of spatially separated light sources was analyzed, as opposed to a single one. Two methods for wind estimation based on the AOA cross-correlation function are presented – the time-delay-to-peak and the slope-at-zero-lag method. This thesis is organized in the form of seven chapters including the current chapter. In Chapter 2, a brief introduction to optical wave propagation and AOA anemometry is provided. Chapter 3 deals with the experimental setup that was used to obtain remote and in-situ wind measurements. In Chapter 4, the specifics of all data processing routines are discussed. In Chapter 5, the results of remote wind measurements are presented alongside a comparison with in-situ measurements. Chapter 6 includes brief discussions on the relative merits and demerits of the two wind estimators and the effects of noise on their performance. Chapter 7 presents some conclusions and an outlook for possible future work.

CHAPTER 2

OPTICAL PROPAGATION THROUGH THE
TURBULENT ATMOSPHERE

In this chapter a brief introduction to optical propagation through the turbulent atmosphere is presented. First, a short mathematical treatment which relates optical AOAs and the optical refractive index is presented. Subsequently, the concept of AOA anemometry is discussed in brief.

2.1 Refractive Index Irregularities and Optical AOAs

Within the framework of geometrical optics, electromagnetic waves propagating through the atmosphere can be treated as bundles of energy traveling along a straight or curved path in the direction of propagation. This gives a notion of a 'ray' traveling along the direction of propagation. Refractive index fluctuations transverse to the nominal ray trajectory of an electromagnetic wave cause the ray path to wander due to refractive bending as shown in Figure 2.1. The integrated effect of many such small refractive bendings produces angular deviations between the tangent vector to the actual ray path and the nominal ray path. These angular deviations in the horizontal and vertical planes are denoted by the angles β and α, respectively. To see how the AOAs are related to the physical parameters (refractive index n) of the propagation medium, a coordinate system is established.
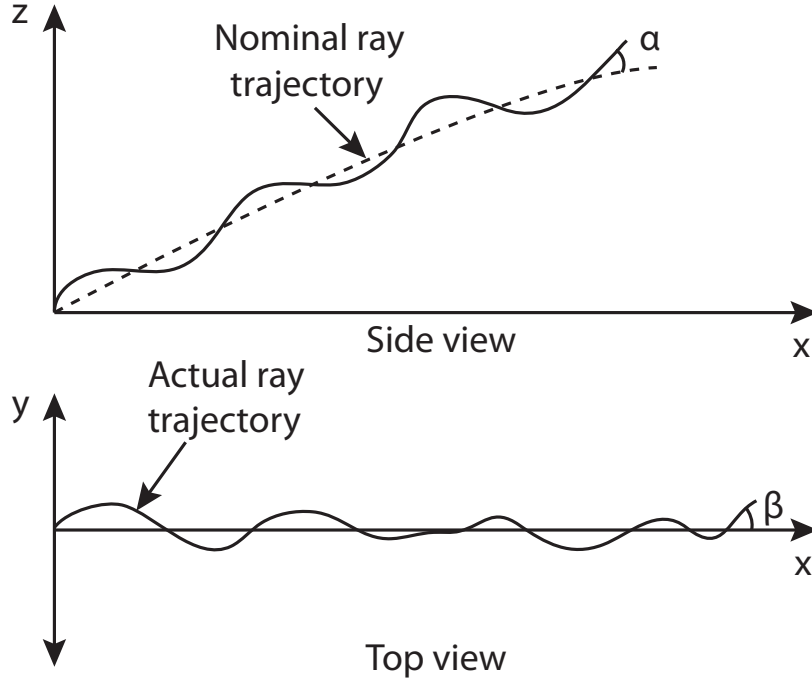
Figure 2.1. Horizontal and vertical angles of arrival. Deviations in the ray path from the nominal trajectory occur due to fluctuations of the refractive index along the ray path, the instantaneous values of which at any point constitute the horizontal AOA – β and the vertical AOA – α in their respective planes.

Consider a right handed coordinate system with the x coordinate along the direction of travel of the ray path, z coordinate along the vertically upward direction, which automatically fixes the y coordinate transverse to the straight line joining the transmitter and receiver as shown in Figure 2.1. Let s represent the coordinate along the direction of the nominal ray trajectory. As a starting point, consider the ray-trajectory Equation 3.10 in [21] which is established using the eikonal solution of the Helmholtz equation. This equation is rewritten to include the effect of the optical refractive index, which yields the following:

$$\frac{d}{ds}\left(n(\vec{r})\frac{d\vec{r}}{ds}\right) = \nabla[n(\vec{r})] \tag{2.1}$$

where $\vec{r}$ is the position vector of a point on the ray trajectory. For obtaining the angular deviation along the transverse (y axis) direction, consider the appropriate coordinate in the above equation along with the perturbed value of the refractive index n. This yields:

$$\frac{d}{ds}\left(\frac{dy}{ds}(\bar{n}+\tilde{n})\right) = \frac{\partial}{\partial y}(\bar{n}+\tilde{n}) \tag{2.2}$$

Because $\tilde{n}$ is typically to the order of 300 ppm (parts per million), one can safely neglect the term $\tilde{n}$ with respect to $\bar{n}$ ($\approx$ 1) on the left hand side of Equation 2.2, after which subsequent integration leads to the expression for the horizontal AOA – β as:

$$\beta = \frac{dy}{ds} = \frac{1}{\bar{n}} \int_T^R \frac{\partial \tilde{n}(x,y,z;t)}{\partial y}\, ds \tag{2.3}$$

where T and R denote the transmitter and receiver locations, respectively.

Similarly for the vertical direction (z axis), appropriate coordinates from Equation 2.1 are considered and subjected to a similar procedure which yields the following expression for the vertical angle of arrival α:

$$\alpha = \frac{dz}{ds} = \frac{1}{\bar{n}} \int_T^R \frac{\partial \tilde{n}(x,y,z;t)}{\partial z}\, ds \tag{2.4}$$

In the above expressions for the AOAs, $\bar{n}$, the nominal value of the optical refractive index of air can be taken as unity. Then, combining Equations 2.3 and 2.4, the total AOA vector can be related to the normal component of the gradient of refractive index fluctuations integrated along the ray path as follows:

$$\vec{\gamma} = \int_T^R \nabla_\perp \tilde{n}(x,y,z;t)\, ds \tag{2.5}$$

where $\vec{\gamma}$ is the total AOA vector (β, α) and $\nabla_\perp$ is the vector $(\frac{\partial}{\partial y}, \frac{\partial}{\partial z})$.

2.2 AOA Anemometry

Consider an optical receiver in the form of a horizontal slit arranged along the transverse coordinate (y coordinate of Figure 2.1). For spherical waves propagating along a path of length, L, the instantaneous, horizontal AOA, at a point on this receiver, in accordance with the coordinate system of Figure 2.1, can be given as:

$$\beta(y; t) = \int_{x=0}^{L} \frac{\partial \tilde{n}(x, y\frac{x}{L}; t)}{\partial y} \, dx \tag{2.6}$$

Assuming stationarity, the spatio-temporal cross-covariance function of the AOAs can then be given by:

$$C_{\beta_1\beta_2}(y, y'; \tau) = \langle \beta_1(y; t)\beta_2(y'; t + \tau) \rangle$$

$$\Rightarrow C_{\beta_1\beta_2}(y, y'; \tau) = \left\langle \int_{x=0}^{L} \frac{\partial \tilde{n}(x, y\frac{x}{L}; t)}{\partial y} \, dx \int_{x'=0}^{L} \frac{\partial \tilde{n}(x', y'\frac{x'}{L}; t + \tau)}{\partial y'} \, dx' \right\rangle$$

$$\Rightarrow C_{\beta_1\beta_2}(y, y'; \tau) = \int_{x=0}^{L} \int_{x'=0}^{L} \left\langle \frac{\partial \tilde{n}(x, y\frac{x}{L}; t)}{\partial y} \frac{\partial \tilde{n}(x', y'\frac{x'}{L}; t + \tau)}{\partial y'} \right\rangle \, dx dx' \tag{2.7}$$

Because refractive index fluctuations along the propagation path can be assumed to be delta correlated (pp. 374–377 in [18]), the term within the angled brackets above can be written as:

$$\left\langle \frac{\partial \tilde{n}(x, y\frac{x}{L}; t)}{\partial y} \frac{\partial \tilde{n}(x', y'\frac{x'}{L}; t + \tau)}{\partial y'} \right\rangle = \delta(x - x')F(y - y'; \tau) \tag{2.8}$$

where $F(y; \tau)$ represents the spatio-temporal cross-covariance of the gradient of the refractive index in the transverse direction, with the range weighting due to spherical

waves and the effect of the partial overlap of ray cones taken into account. The function $F(y; \tau)$ can be obtained by integrating Equation 2.8 over x' as follows:

$$F(y - y'; \tau) = \int_{x'=0}^{L} \left\langle \frac{\partial \tilde{n}(x, y\frac{x}{L}; t)}{\partial y} \frac{\partial \tilde{n}(x', y'\frac{x'}{L}; t + \tau)}{\partial y'} \right\rangle dx' \qquad (2.9)$$

Using Taylor's frozen turbulence hypothesis [19], it can be argued that the behavior of the refractive index fluctuation at a certain point in space is determined by its behavior at a previous position at a delayed time. In other words:

$$\frac{\partial \tilde{n}(x', y'\frac{x'}{L}; t + \tau)}{\partial y'} = \frac{\partial \tilde{n}(x', y'\frac{x'}{L} - v\tau; t)}{\partial y'} \qquad (2.10)$$

where v is the transverse velocity of the wind blowing across the propagation path.

Using Equation 2.10 in Equation 2.9, the following is obtained:

$$F(y - y'; \tau) = \int_{x'=0}^{L} \left\langle \frac{\partial \tilde{n}(x, y\frac{x}{L}; t)}{\partial y} \frac{\partial \tilde{n}(x', y'\frac{x'}{L} - v\tau; t)}{\partial y'} \right\rangle dx' \qquad (2.11)$$

This equation is the starting point in the extraction of the transverse wind velocity from horizontal AOAs using two methods – the time-delay-to-peak and the slope-at-zero-lag (of the AOA cross-correlation function). From Equations 2.11 and 2.7, it is evident that the peak of the AOA cross-correlation function will coincide with that of the transverse refractive index gradient cross-correlation function. Physically, the time delay to the peak of the transverse refractive index gradient cross-correlation function represents the time taken by eddies to advect over a certain distance (the effective source/receiver separation – which is determined by the geometry of the problem). Hence, when this effective separation and the time delay to the peak of the AOA cross-correlation function are known, the transverse wind velocity can be easily determined. The basis of the second method – the slope-at-zero-lag method, can be

8

seen upon differentiating Equation 2.11 with respect to τ and then setting τ to zero, which causes the velocity term to appear outside the integral. In other words, the slope at zero lag of the AOA cross-correlation function is also directly proportional to the transverse wind velocity. Empirical results obtained using the above two methods are presented in Chapter 5.

CHAPTER 3

EXPERIMENT AND INSTRUMENTATION SETUP

This chapter describes the various components of the experimental setup that were employed for the acquisition of atmospheric data. First, a brief account of the experiment site – the Boulder Atmospheric Observatory and the instrumentation setup are presented. This is followed by detailed sections describing the setup and operation of the sonic towers and the telescope-LED light component.

The data used in analyses described in subsequent parts of this thesis was collected as a part of a field experiment carried out over a period of eleven days from 7 to 18 June, 2010. The location for this field campaign was the Boulder Atmospheric Observatory (BAO) site near Erie, Colorado. The BAO is a research facility operated by the National Oceanic and Atmospheric Administration (NOAA) and includes a tower, 300 m high (not used as a part of the experimental setup described in this thesis), to mount sensors for collecting atmospheric data. The majority of the land within the facility was covered by dry bush which varied in height from 30 cm to 90 cm. A major part of the experiment involving sonic towers and the optical instrumentation was carried out in the area south-west of the BAO tower. Calibration of the sonics was carried out at the calibration stand near the BAO tower prior to their being mounted on the sonic towers. Figure 3.1 shows a plan view of the experimental setup at the BAO site.

Figure 3.1. Plan view of the experimental setup at the BAO site. The 300 m high tower can be seen in the top right corner of the image. The area south-west of this tower was used to setup the entire instrumentation. The individual components are indicated by red markers, the features and locations of which are listed in the key to the top right corner of the image.

The optical propagation path as indicated by the top (L1) and bottom (T1) red markers of Figure 3.1, was 182 m long. At the two ends of this path were placed a Schmidt-Cassegrain type telescope (T1) and a rectangular array of LED lights (L1). Along this propagation path were placed two sonic towers, the separation between them being 61 m. The first sonic tower (ST1) had sonics mounted on six levels and was at a distance of 47 m from the telescope. The second sonic tower (ST2) had three levels with two sonics mounted on each level and was at a distance of 74 m from the rectangular array of LED lights. This is illustrated by Figure 3.2.
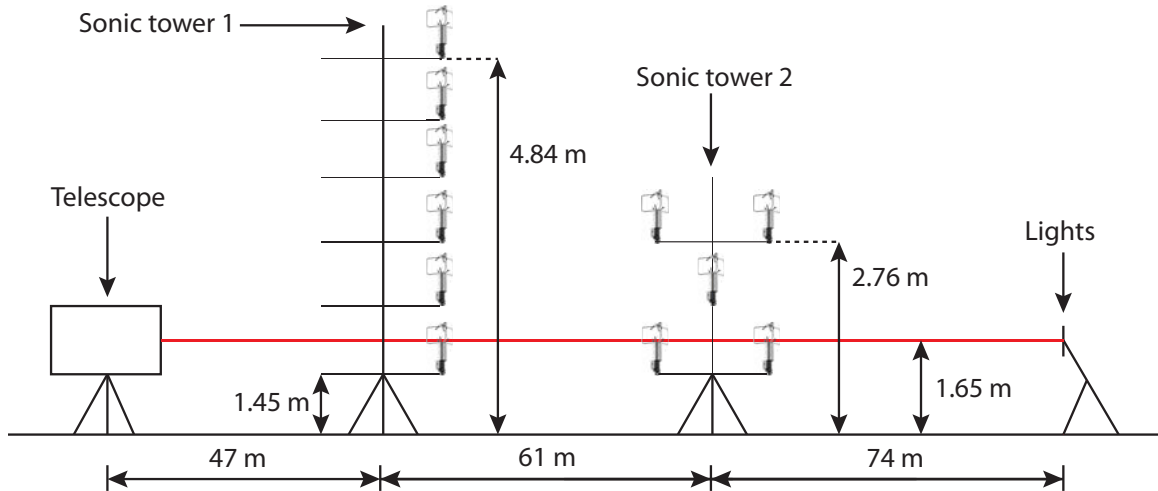
Figure 3.2. Side view of the experimental setup at the BAO site. The optical propagation path as defined by the telescope and LED lights was 182 m. Along this path were also placed two towers mounted with sonics at various levels between 1.45 and 4.84 m AGL.

3.1 Sonic Towers

Two sonic towers were erected as part of the field experiment as shown in Figure 3.2. On each of the towers were mounted ultrasonic anemometer-thermometers (sonics) (Model 81000, manufactured by R. M. Young Company of Traverse City, Michigan). The sonic is a three axis meteorological sensor which measures the three wind vectors, u, v and w and the temperature, T. It has three ultrasonic transmitter-receiver pairs, which are separated by $120°$ in azimuth and arranged at an elevation angle of $60°$ from the vertical axis of the device. The sonic operational configuration was set so as to have a measurable wind speed range of 0 to $40\,\mathrm{ms}^{-1}$ with a resolution of $0.01\,\mathrm{ms}^{-1}$. Its measurable temperature range was -50 to $+50\,°\mathrm{C}$ with a resolution of $0.01\,°\mathrm{C}$. Six sonics were mounted on Tower 1 at various levels between 1.45 and 4.84 m AGL as shown in Figure 3.3.

Figure 3.3. Front view of Tower 1. The central framework of the tower is a metal bar which rests on a firmly secured tripod. Crossbars mounted at various levels between 1.45 and 4.84 m AGL have sonics attached to their ends. Apart from sonics one can also see the inlets of the barometers and a GPS antenna mounted on the tower. The white box laying beside the base of the tower contains the data-logger.

Tower 1 was located at $40.04581°$ N, $105.00638°$ W. In addition to six sonics mounted at levels of $145, 213, 281, 348, 416, 484$ cm AGL, it also had two quartz crystal barometers (Intelligent Transmitters Series 6000) (manufactured by Paroscientific, Inc., Redmond, Washington) with their inlets mounted at levels 150 and 349 cm AGL. Adhering to the R. M. Young convention, all of the sonics mounted on Tower 1 had their electronic black boxes facing towards north. This resulted in the u component of the three dimensional wind vector to be the transverse wind blowing across the propagation path for Tower 1 sonics. Wind blowing from the east to the west (right to left in Figure 3.1) was recorded with a positive value for the u component according to the R. M. Young convention.

Tower 2 was located 61 m north of the first tower along the propagation path. Tower 2 had six sonics mounted in pairs on either sides of booms at levels of $142, 209, 276$ cm AGL (the middle boom was arranged transverse to the booms above and below it and it was approximately transverse to the optical propagation path). The sonics mounted on the top and bottom crossbars had their electronic black boxes pointing towards north, while the ones on the middle bar had them facing towards east. Hence, for the four sonics on the top and bottom levels of Tower 2, the u component represented the transverse wind, and for the sonics on the middle crossbar, it was the v component that represented the transverse wind blowing across the propagation path. For the sonics on the middle crossbar, wind blowing from the east to the west (right to left in Figure 3.1) was recorded with a positive value for the v component according to the R. M. Young convention.

All barometer and sonic data on both the towers were collected by means of custom built data-loggers, the detailed construction of which can be found in [1]. Each

data-logger contains a stand alone computer system running on a Linux based operating system. It also contains an 8-to-1 Serial-to-USB adapter which is capable of collecting data from 8 sensors operating simultaneously at their maximum sampling rate. The logging software (also developed in part by Behn *et al.* [1]) assigns UTC (Coordinated Universal Time) stamps to data from each channel. The timing accuracy is maintained by having the system clock of the data-logger in continuous synchronization with UTC by means of NTP (Network Time Protocol) functionality embedded within the Linux based operating system that was running on the data-logger. A GPS antenna and an on board receiver were used to provide continuous timing information to the NTP program for updating the system clock with UTC with an accuracy of up to a few micro-seconds. All of the sonic and barometer data was stored on a 160 GB magnetic hard drive located within each data-logger.

3.2   Telescope and LED Lights

A large-aperture telescope (Model LX200GPS, Schmidt-Cassegrain type, manufactured by Meade Instruments Corporation of Irvine, California) was set up at the southern end of the optical propagation path at 40.04536° N, 105.00636° W. Tower 1 was located 47 m north of the telescope as shown in Figure 3.2. The tripod of the telescope rested on concrete blocks to prevent the legs from sinking into the soil. The center of the telescope aperture was at a height of 1.77 m AGL. The telescope along with its tripod stand is shown in Figure 3.4.

Figure 3.4. Side view of the telescope. Attached to the telescope is a CCD-camera, which collected 30 images per second. These images were saved on a laptop PC.

On the top left corner of the telescope (when looking into the telescope), one can see the auxiliary telescope. This was used initially after the telescope was setup, to bring the LED light array into the field of view. A black-and-white CCD-camera (Model 075M, manufactured by Lumenera Corporation of Ottawa, Ontario, Canada) was mounted at the rear-side observation port of the telescope for capturing images of a rectangular array of four test lights. The photographic plate of the CCD-camera had 640×480 pixels, with a pixel width of $7.4\,\mu$m in both directions. The CCD-camera was directly connected to a laptop computer via a USB interface. The laptop was running the software (Stream Pix) which controlled the exposure settings of the camera and also collected images from it, which were locally stored on the hard drive of the laptop computer.
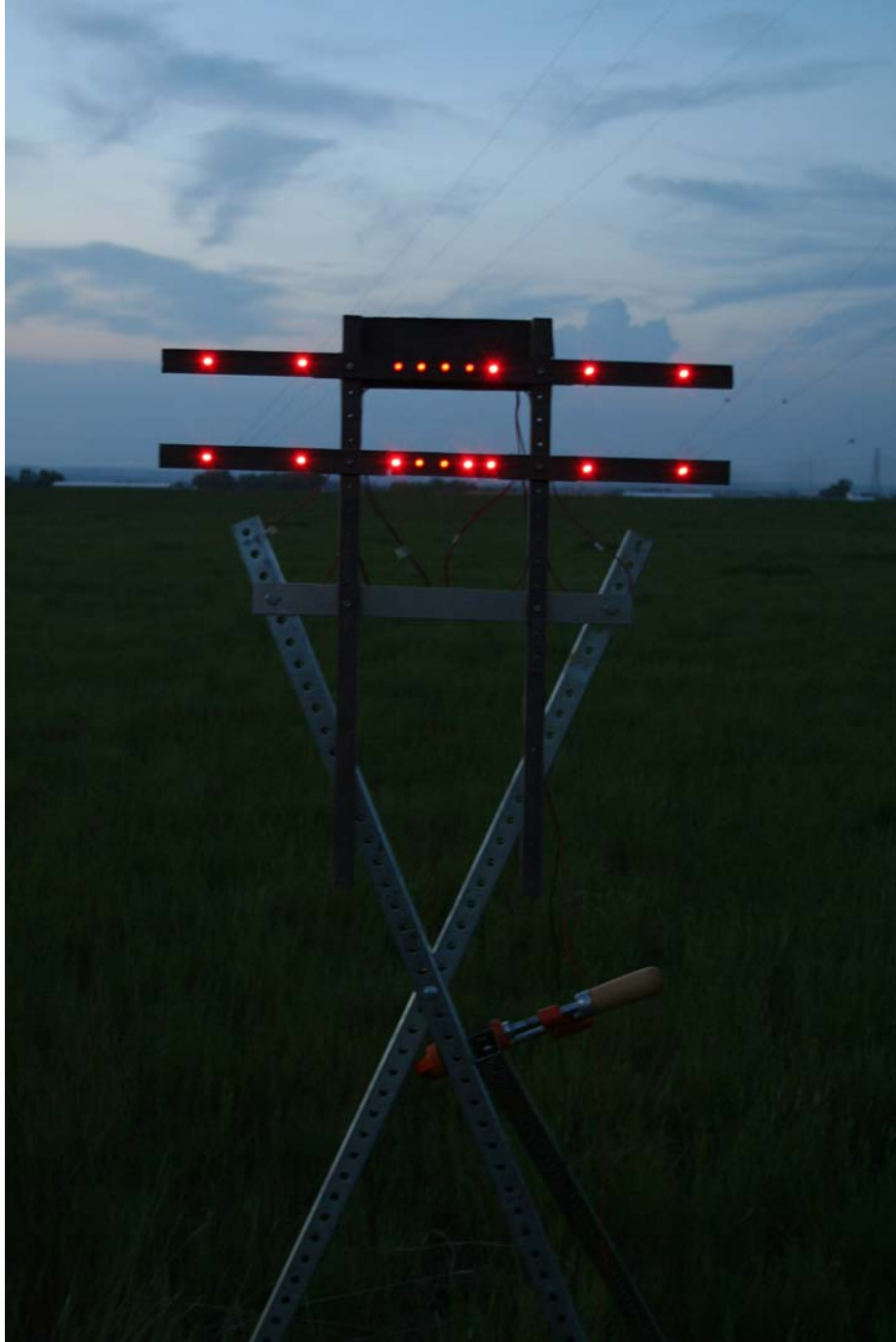
Figure 3.5. The LED light array mounted on a sturdy metal stand. The light stand was placed 182 m north of the telescope. The rectangular array of size 10 cm by 7.5 cm as seen in the upper right corner of the LED array was observed through the telescope.

Four LED lights, approximately 4 mm in diameter were arranged at the corners of a rectangle, 10 cm in length and 7.5 cm in width, as shown in Figure 3.5. This was part of an adjustable assembly of LED lights that were mounted on a sturdy metal support and placed 182 m north of the telescope at the location 40.04699° N, 105.00625° W. The optical propagation path was parallel to and about 2 m east of the baseline defined by the main poles of Tower 1 and Tower 2. The center of the LED array was positioned 1.77 m AGL.

The auxiliary telescope mounted on the main telescope was used to manually bring the rectangular light array in the field of view of the main telescope. The CCD-camera was then placed in the view port of the telescope and connected to the laptop computer via a USB cable. The laptop computer ran the software Stream Pix, which was used to view the output of the CCD-camera in real time. The telescope was adjusted until the LED light array was in focus as shown in Figure 3.6.

Refractive index irregularities that advect along with the wind as it blows across the lights cause the images to quiver in the focal plane of the telescope. This causes the boundaries of the light images to blur and places a limit on the achievable degree of focusing of the telescope. Hence, reasonably sharp image boundaries of the lights were taken as an indicator of the telescope being focused on the LED light array. Once this was done, the software Stream Pix was used to set the parameters for the CCD-camera operation such as the exposure time, frame rate, duration etc. Images were collected for about 9 h beginning at about 2035 MDT on June 15, 2010, in the form of five segments, each of approximately 2 h duration.
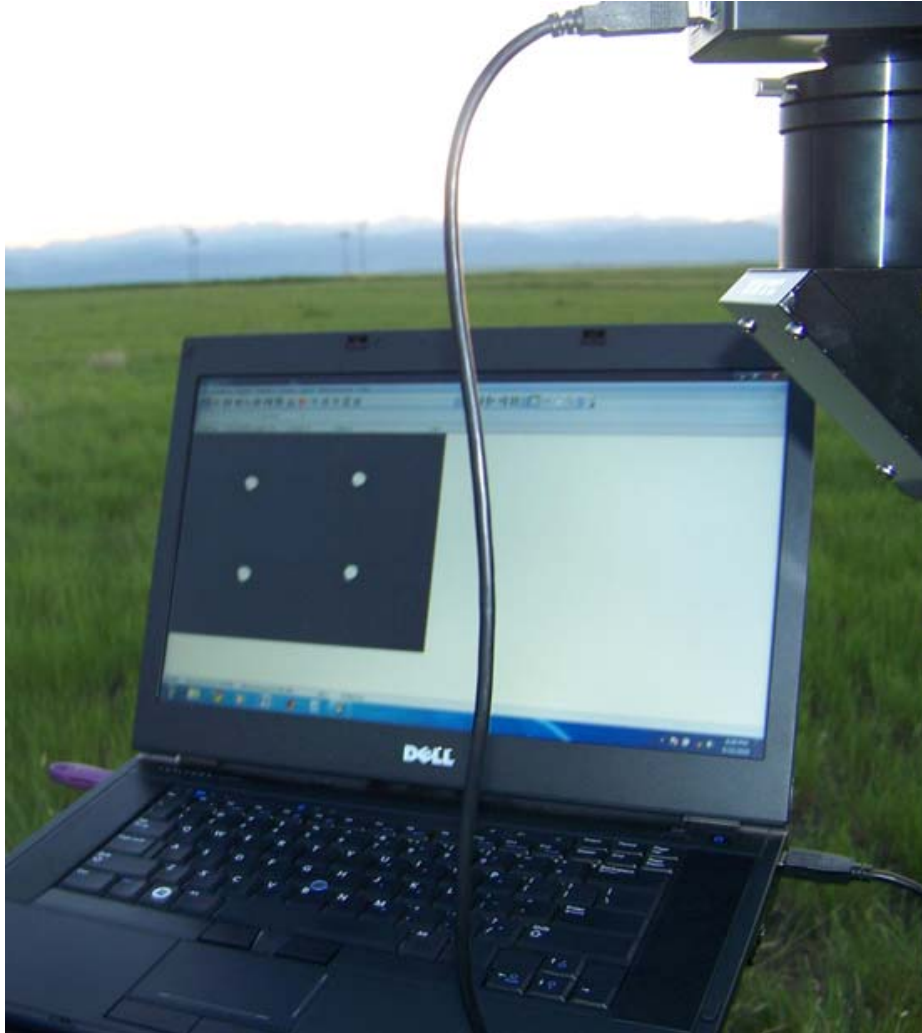
Figure 3.6. The rectangular LED light array as observed through the CCD-camera attached to the telescope. This image is viewed through Stream Pix. The boundaries of the lights appear reasonably sharp indicating that the telescope has been focused well on the light array. But one can still observe slight deformation of the otherwise circular images and this can be attributed to the random refractive-index fluctuations due to atmospheric turbulence along the propagation path.

CHAPTER 4

DATA PROCESSING

In this chapter, various aspects of data processing that go into the extraction of parameters which lead to the estimation of the transverse horizontal wind velocity are presented. First, the procedure for obtaining AOAs from image sequences collected by the CCD-camera is described. The procedure for evaluating the AOA cross-correlation function between β_1 and β_2 – the AOAs from two horizontally separated light sources, follows. Then, the procedures for obtaining the two estimators for remote wind retrievals – the time delay to the peak and the slope at zero lag of the AOA cross-correlation, are described. This is followed by a brief account of the sonic data processing.

4.1 Estimation of the AOAs

Raw data that was obtained from the CCD-camera attached to the telescope was stored as a sequence of FIT (Flexible Image Transport) images by Stream Pix. These unprocessed image sequences were stored on the internal hard drive of the laptop computer which controlled the CCD-camera operation via Stream Pix. MATLAB routines were subsequently used to obtain centroid positions for each of the four lights from these image sequences. These centroid extraction routines divided each image into four zones corresponding to each LED light in the array. For each zone, the centroid was computed by sequentially running through all the pixels in that zone and determining whether a pixel was the brightest amongst others within a fixed distance from it. The initial values of the centroids were stored and used as reference

positions in subsequent zone scans to increase computational efficiency. The obtained centroid pixel coordinates were segregated along the two axes corresponding to the orientation of the CCD-camera photographic plate. Pixel coordinates along the horizontal direction were treated as y coordinates, while those along the vertical direction were treated as z coordinates. This lead to a natural selection for the propagation path to be along the x axis.

Centroids obtained using the above procedure were stored as two four-column matrices, one each for the y and z directions. The transition from centroids to AOAs was made by using the following argument. For the experimental setup as illustrated before, the aperture diameter of the telescope is $D = 36\,\mathrm{cm}$, the wavelength of red light is $\lambda = 700\,\mathrm{nm}$, and the length of the optical propagation path is $L = 182\,\mathrm{m}$. Using these numbers, it is seen that the condition $D \gg \sqrt{\lambda L}$ is satisfied. In other words, the diameter of the telescope aperture is big enough so that diffraction effects may be neglected. Hence, if it is assumed for simplicity that the LED lights are point sources, then, given that the telescope is focused on these point sources, the LED lights are observed as point images in the focal plane of the telescope. For a point image in the focal plane of the telescope having pixel coordinates i and j, the corresponding AOAs can be obtained as follows:

$$
\begin{pmatrix} \beta \\ \alpha \end{pmatrix} = \frac{1}{F} \begin{pmatrix} \Delta_y i \\ \Delta_z j \end{pmatrix} = \begin{pmatrix} \Delta_\beta i \\ \Delta_\alpha j \end{pmatrix}
\tag{4.1}
$$

where F is the focal length of the telescope and Δ_y, Δ_z are the pixel spacings of the CCD-camera photographic plate in the y and z directions, respectively. Using, $F = 3.556\,\mathrm{m}$ and $\Delta_y = \Delta_z = 7.4\,\mu\mathrm{m}$, a horizontal and vertical angular pixel resolution of $\Delta_\beta = \Delta_\alpha = 2.08\,\mu\mathrm{rad}$ is obtained. More details regarding the above can be found in [5].

4.2 The AOA Cross-Correlation Function

The AOAs obtained using the procedure illustrated in Section 4.1 are discrete time sequences. For convenience purposes, let β_1 and β_2 represent the horizontal AOA signals from the lower left light and lower right light, respectively, of the rectangular LED array. Then, the discrete time cross-correlation function between β_1 and β_2 can be given by:

$$B_{\beta_1\beta_2}[m] = \frac{\frac{1}{L}\sum_{i=1}^{L}\tilde{\beta}_1[i]\tilde{\beta}_2[i+m]}{\sqrt{\sigma_{\tilde{\beta}_1}^2\,\sigma_{\tilde{\beta}_2}^2}} \tag{4.2}$$

where m is the sample shift and L is the number of samples over which the cross-correlation function is calculated.

The tilde on β_1 and β_2 indicate that both are mean removed quantities (i.e. only fluctuations). The maximum relative sample shift between β_1 and β_2 for the analyses described herein, was kept equivalent to a time shift of ± 2 s, while the number of samples L was kept equivalent to a time period of 10 s. This equivalence between continuous times and integer sample numbers was obtained by taking into consideration the effective rate at which the CCD-camera photographic plate was sampled by Stream Pix (≈ 30 Hz). It should be noted that the discrete time AOA cross-correlation function as calculated in Equation (4.2) is a function of the integer sample shift, m. The discrete time AOA cross-correlation as a function of the time shift, τ ($B_{\beta_1\beta_2}(\tau)$) can be obtained simply by a translation of the integer sample shift axis to the time shift axis. This is accomplished by the use of the effective sampling interval, T to relate the integer sample shift, m and the time shift, τ, by $\tau = mT$. The above calculations for the discrete time AOA cross-correlation function are done in the time domain, such that the two optical wind estimation parameters (to be described in the following sections) can be obtained directly. The cross-correlation is computed for a maximum time shift of $\tau = \pm 2$ s for each 10 s segment pair of β_1 and β_2.

For calculating the AOA cross-correlation function, 10 s long segments of both, β_1 and β_2 are formed. Because the calculation is carried out for a maximum time shift of $\tau = \pm 2$ s, an equivalent amount of samples are appended on either side of both the 10 s long AOA segments. This avoids the deficiency of AOA values within the 10 s interval when one signal is shifted with respect to the other. The two 14 s long AOA segments are then multiplied (element-by-element) and shifted successively. After each multiply operation, the products over the original 10 s overlap are accumulated and stored as the cross-covariance for the corresponding time shift, τ. This quantity is normalized by the product of the standard deviation of the two AOA segments to yield the cross-correlation. The same is repeated for all values of the time shift, τ between -2 and $+2$ s to yield the AOA cross-correlation function for a 10 s duration.

4.3   Optical Wind Estimation

This section describes the two routines employed for obtaining parameters that yield estimates of the transverse horizontal wind velocity, namely the time delay to the peak and the slope at zero lag of the AOA cross-correlation function.

4.3.1   Time Delay to the Peak of the AOA Cross-Correlation Function

The time delay to the peak of the AOA cross-correlation function is one of the estimates used to determine the transverse horizontal wind velocity [12]. Once the AOA cross-correlation function has been obtained as described in Section 4.2, its peak is found by traversing the cross-correlation values for each 10 s long segment. Once found, three points around and including the peak are used to fit a parabolic curve around the peak of AOA cross-correlation function, i.e. $B_{\beta_1 \beta_2}(\tau) = a\tau^2 + b\tau + c$. The time delay to the peak, τ_p is then found by setting the first derivative of the above curve to zero as follows:

$$\tau_p = -\frac{b}{2a} \tag{4.3}$$

23

Once the time delay to the peak of the AOA cross-correlation function has been obtained, Taylor's frozen turbulence hypothesis can be invoked to estimate the transverse horizontal wind velocity [19]. Before this is done, the effective light separation needs to be determined, because the LEDs, instead of producing collimated beams, produce diverging spherical wavefronts which lead to overlapping ray cones over the propagation path. Hence, one cannot directly assume a separation of $d/2$ (where d is the physical light separation) which would be the case with collimated beams. Because the ray cones overlap over the propagation path, it is to be expected that the effective separation coefficient is less than 0.5. This effective spacing parameter, γ_1, is obtained by a calibration process. The transverse horizontal wind velocity measured by the sonics at the level of the propagation path, v_s is used for this calibration process. Using Taylor's frozen turbulence hypothesis, the beam transverse horizontal wind velocity can be given as:

$$v_t = \gamma_1 \frac{d}{\tau_p} \tag{4.4}$$

4.3.2 Slope at Zero Lag of the AOA Cross-Correlation Function

The second parameter used in the estimation of the transverse horizontal wind velocity is the slope at zero lag of the AOA cross-correlation function [14][13]. To obtain this parameter, four points around and including the value of the AOA cross-correlation at zero lag ($\tau = 0$) are selected and used to fit a polynomial in the third degree, i.e. $B_{\beta_1\beta_2}(\tau) = p\tau^3 + q\tau^2 + r\tau + s$. This curve is then differentiated with respect to τ and evaluated at $\tau = 0$ to get the slope at zero lag of the AOA cross-correlation function. To make this quantity insensitive to fluctuations of the refractive index structure parameter, C_n^2 along the propagation path, it is divided by the value of the AOA cross-correlation at zero lag [14]. This results in the following:

$$\frac{\left.\frac{\partial B_{\beta_1\beta_2}(\tau)}{\partial \tau}\right|_{\tau=0}}{B_{\beta_1\beta_2}(0)} = \frac{r}{s} \tag{4.5}$$

24

The linear relationship between the transverse horizontal wind velocity and the slope at zero lag of the AOA cross-correlation function is well known from [13]. Similar to the time-delay-to-peak method, the sonic velocity measured at the level of the propagation path, v_s, is used to calibrate for γ_2 – the constant of proportionality for this linear relationship. The beam transverse horizontal wind velocity can be then given as:

$$v_t = \gamma_2 \frac{\left.\frac{\partial B_{\beta_1\beta_2}(\tau)}{\partial \tau}\right|_{\tau=0}}{B_{\beta_1\beta_2}(0)} \tag{4.6}$$

4.4 Sonic Data Processing

Throughout the entire experimental run, data from all the sonics was collected via custom built data-loggers developed by Behn *et al.* [1]. Sonic data in the form of the three wind vectors, u, v and w, the temperature, T, along with the time stamp created by the data-logging software was stored as lines of ASCII text in files with the extension '*.dat*'. Pre-developed MATLAB routines were used to convert these '*.dat*' files into files of type '*.mat*'. Apart from this conversion functionality, the routines also served the purposes of error checking and invalid format corrections. The resulting '*.mat*' files contained six vectors corresponding to the three wind components, u, v and w, the temperature, T, the time in UTC, t and the time in EST, tm. Because the sonics sampled at a non-uniform rate of $\approx 32\,\text{Hz}$, all data was subject to pre-processing in which it was interpolated to an equidistant grid corresponding to a sampling frequency of $30\,\text{Hz}$.

Six sonics from the experimental setup were in the immediate vicinity of the optical propagation path (at $1.77\,\text{m}$ AGL). These included two sonics from Tower 1 – #02288 and #01473 at 1.45 and $2.13\,\text{m}$ AGL, respectively and four sonics from Tower 2 – #02158, #02151 and #01530, #02157 at 1.42 and $2.09\,\text{m}$ AGL, respectively. The arrangement of the sonics, telescope and the lights was such that both sonics from

Tower 1 and the lower sonics from Tower 2 had their u components of the wind transverse to the optical propagation path, while the middle two sonics from Tower 2 had the v components of the wind transverse to the optical propagation path. These components were retrieved from the sonic data files accordingly for comparison with the optically derived wind velocity values. The directional convention for the wind, as adopted by the manufacturer of the sonic (R. M. Young) was taken into account during this exercise. R. M. Young conventions for the horizontal wind vector are opposite to meteorological conventions. Hence, the sonics measure positive u and v components when the wind blows from the east to west and north to south, respectively. Once this directional antonymy was resolved, segments of the wind vectors were obtained according to the start and end times of the AOA data segments. 10 s averages were subsequently obtained from these so that they may be compared with 10 s optical estimates of the transverse horizontal wind vector.

10 s averages of the wind vectors, u and v from the two levels between which the propagation path lay, were used to compute the transverse horizontal wind velocity at the level of the propagation path. Ideally, this would be achieved by obtaining the logarithmic profile for the wind between the two levels concerned and then interpolating the value of the wind at the level of the propagation path. But, because the two levels were separated by a relatively short height ($\approx 0.7\,\mathrm{m}$), a linear profile was used as an approximation. The propagation path lay approximately midway at $1.77\,\mathrm{m}$ AGL between the two sonic levels at ≈ 1.4 and $\approx 2.1\,\mathrm{m}$ AGL. Hence, the transverse horizontal wind velocity at the level of the propagation path was obtained by taking the mean of the transverse horizontal wind velocities at the levels above and below the propagation path.

CHAPTER 5

RESULTS

In this chapter, results of the two aforementioned optical wind estimation techniques – the time-delay-to-peak and the slope-at-zero-lag methods are presented. The data used in subsequent analyses was recorded over a period of 9 h beginning at approximately 2035 MDT on the night of 15 June, 2010. The optical data over this entire run was collected as five discrete segments, each of approximately 2 h duration. Of the four lights in the rectangular LED light array, the horizontal AOAs from the lower two lights are analyzed. Time series of the angles of arrival – β_1 and β_2 are first presented, followed by the discrete time cross-correlation function between β_1 and β_2, for a 10 s duration. 10 s averages of sonic measured and optically estimated wind velocities are subsequently compared to quantify the accuracy of the two methods employed for optical wind retrievals.

5.1 Angles of Arrival

Image sequences of the lower two lights, for all five segments, were subject to the operations described in Section 4.1. It must be noted that prior to applying these routines, a running average series was subtracted from each of the centroid signals. This was done so as to remove the effect of the position of the light on the photographic plate of the CCD-camera, on the AOA signal magnitude, so that only pixel fluctuations, rather than the absolute pixel positions are obtained. The reason for using the lower two lights in subsequent analyses is as follows. During the night the temperature gradient close to the ground is positive, meaning that the temperature

27

increases with altitude. Therefore, the refractive index of air decreases with altitude. Because light rays bend towards a denser medium, a downward bending of light rays is observed in the nocturnal surface layer. Thus, when viewed through the telescope, the LED lights appear at a position higher than their true positions. As the cooling intensifies over the night, the lights appear to move upward due to stronger refractive bending. Thus, it is more likely for the upper two lights of the rectangular array to go out of view, than the lower pair. Hence, in order to avoid the loss of AOA signals, the lower two lights were selected for analysis. The AOA signals, β_1 and β_2, for two of the five segments recorded are shown below in Figures 5.1 and 5.2.
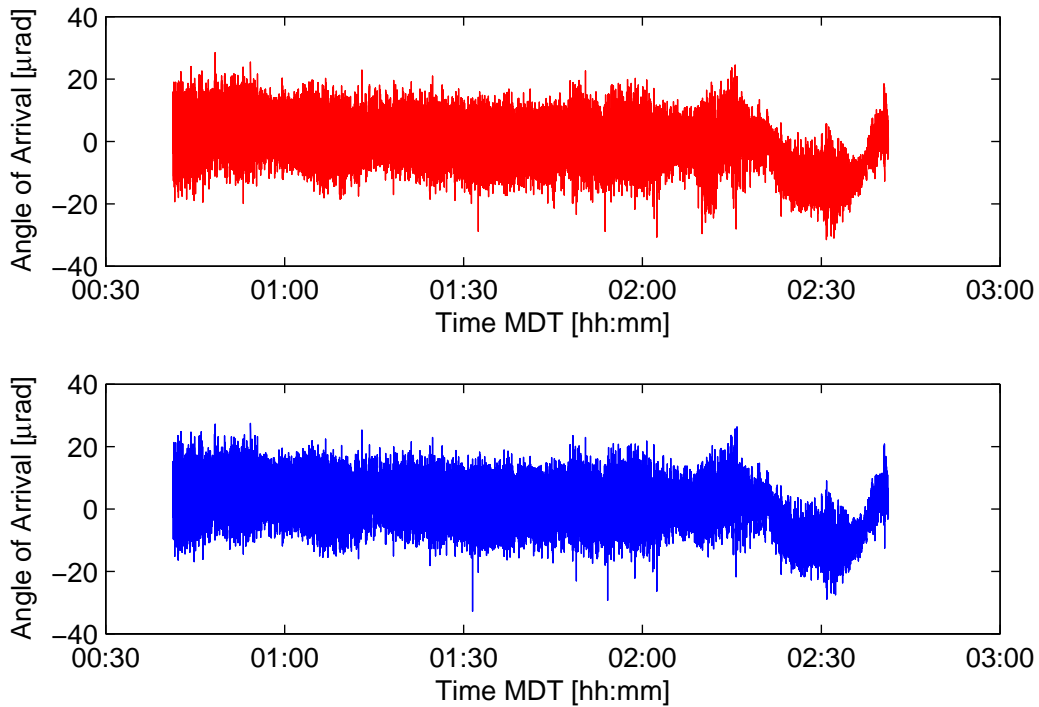
Figure 5.1. Time series of the horizontal angle of arrival, β, for segment 3. Top panel shows the horizontal AOA, β_1 for light 1 (in red). Bottom panel shows the horizontal AOA, β_2, for light 2 (in blue).
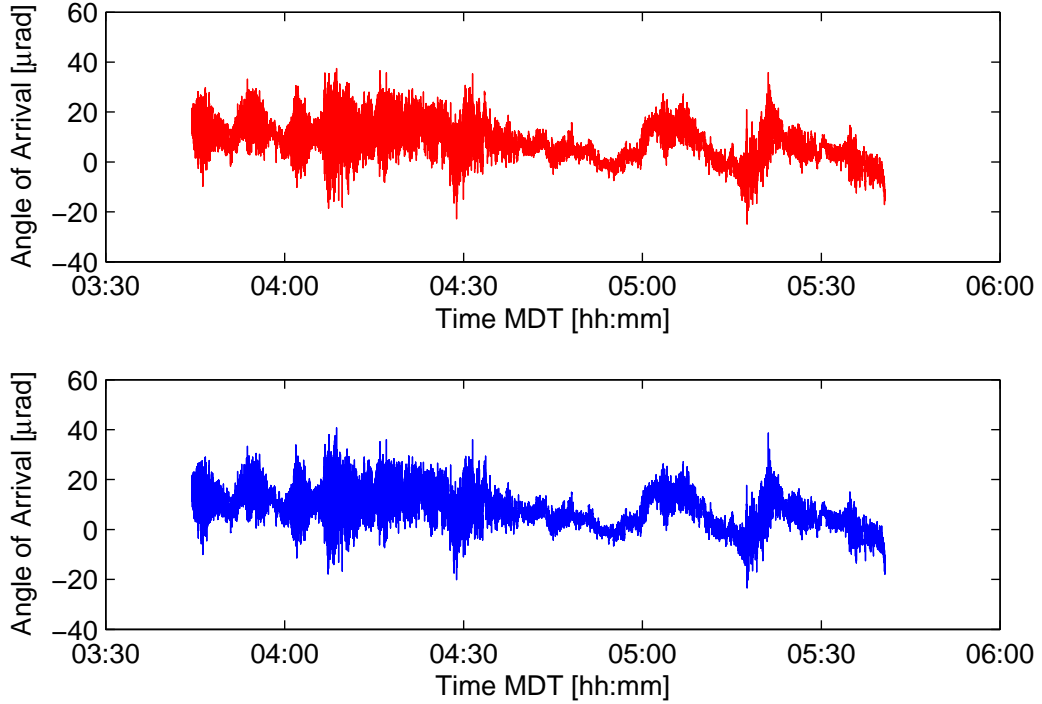
Figure 5.2. Time series of the horizontal angle of arrival, β, for segment 5. Top panel shows the horizontal AOA, β_1 for light 1 (in red). Bottom panel shows the horizontal AOA, β_2, for light 2 (in blue).

During a majority of the period of the experiment, a significant wind was seen to blow from direction of the mountains, which are to the west of the BAO site. This caused fluctuations in β_2 to occur after a slight delay in those of β_1. Thus, β_2 can be expected to lag β_1 for a majority of the overnight data segment. This is indeed the case as seen from a 3 s long zoomed in view of β_1 and β_2 shown in Figure 5.4.

5.2 The AOA Cross-Correlation Function

The discrete time AOA cross-correlation function between β_1 and β_2 is calculated over a period of 10 s as described in Section 4.2. One such instance of the AOA cross-correlation function is calculated for a segment beginning at 0403 MDT. The

two AOA signals β_1 and β_2 for this 10 s long segment are as shown in Figure 5.3. It may be observed that although the AOA cross-correlation function is computed for a 10 s period, the displayed (and segmented) signals β_1 and β_2 are of 14 s duration. This can be attributed to the fact that the maximum value of the time shift τ between β_1 and β_2 is ± 2 s. Buffer periods of 2 s on either ends of both β_1 and β_2, ensure the existence of fully populated vectors corresponding to both the AOA signals over the 10 s duration under consideration.
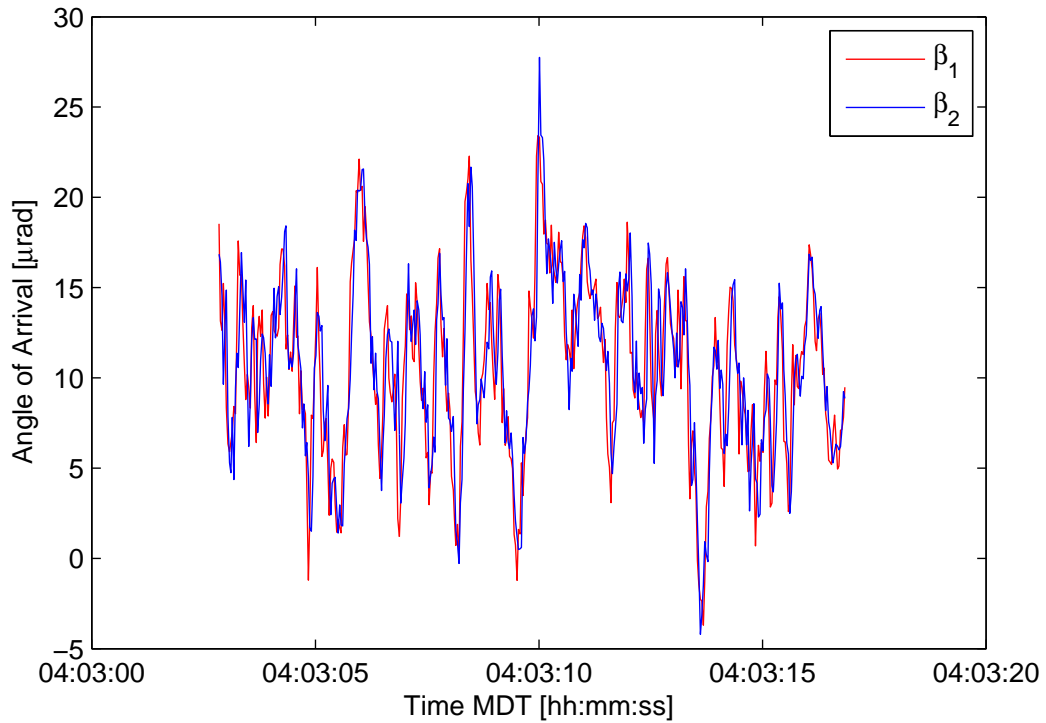
Figure 5.3. β_1 and β_2 segments for AOA cross-correlation function computation. Although the AOA cross-correlation function is computed over a period of 10 s, 14 s long segments are created as shown. The extra 4 s of AOAs are used as 2 s long buffer signals at each end of the 10 s long AOA segment under consideration to account for the maximum value of the time shift τ, which is ± 2 s.
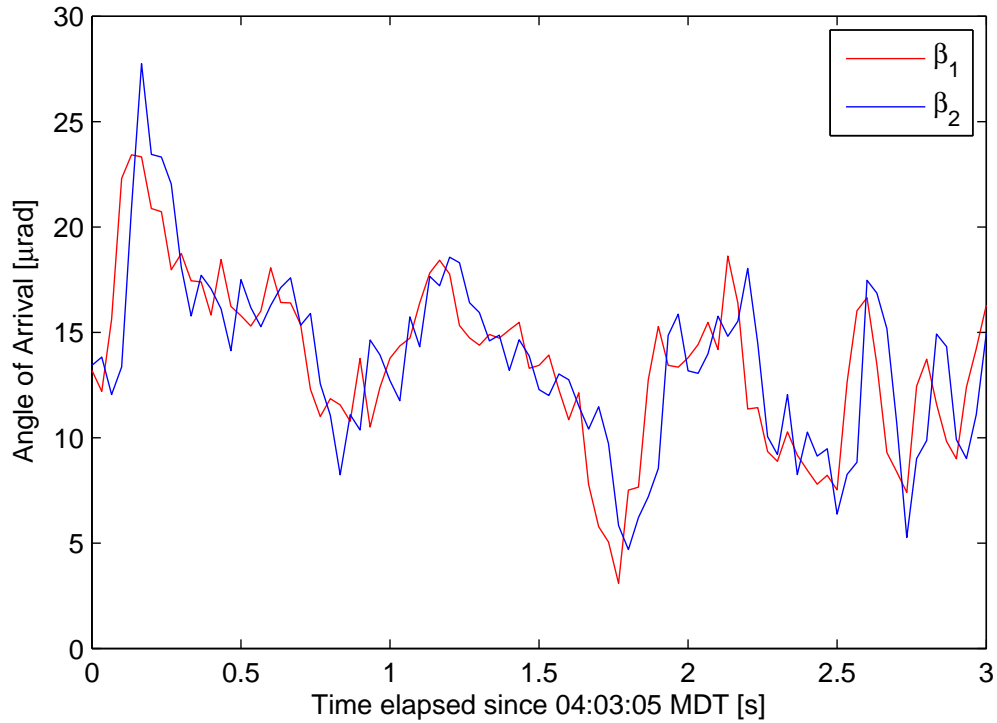
Figure 5.4. A 3 s long zoomed in segment of β_1 and β_2 beginning at 0403 MDT. A positive time delay to the order of a fraction of a second is clearly discernible between the two AOAs, which can be inferred as the result of the wind blowing across the lights from west to east.

A 3 s long view of the same segment is as shown in Figure 5.4. A positive time lag between β_1 and β_2 (β_1 leads β_2) can be clearly seen. This delay can be expected to manifest itself in the form of the time delay to the peak of the AOA cross-correlation function of β_1 and β_2. The AOA cross-correlation function computed for the above 10 s long segment is as shown in Figure 5.5.
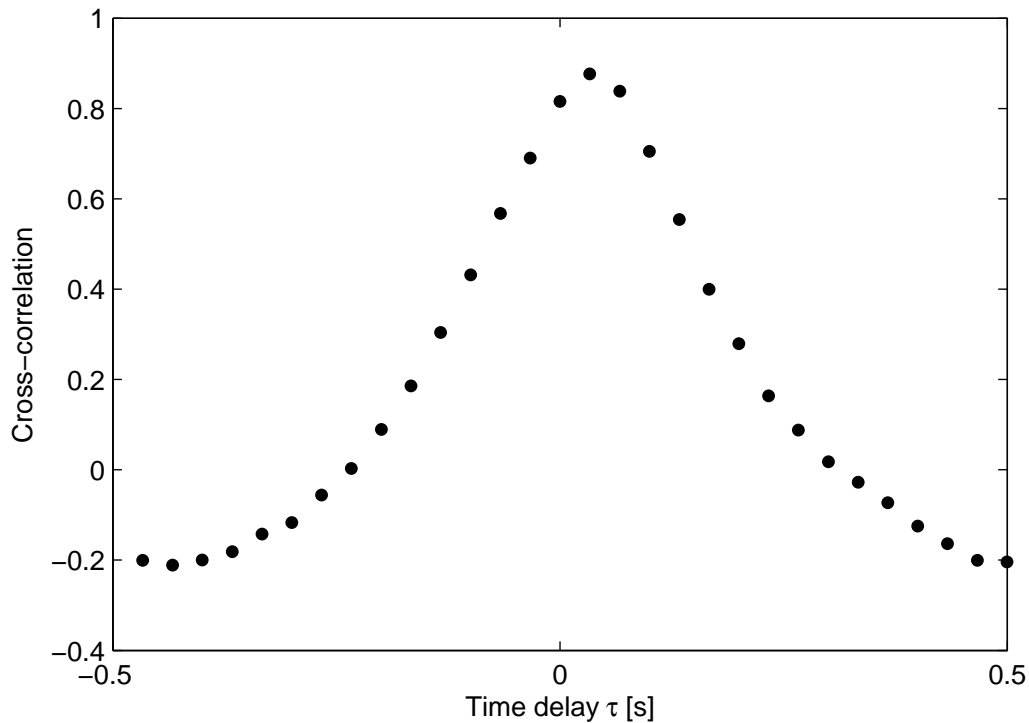
Figure 5.5. The AOA cross-correlation function of β_1 and β_2 at 0403 MDT. Consistent with observations in the previous figure, a fractional time delay to the peak shows up in the AOA cross-correlation function.

As is seen from Figure 5.5, there is a discernible time delay to the peak of the AOA cross-correlation function which is of the order of a fraction of a second. This is consistent with observations illustrated in Figure 5.4.

5.3   Optical Wind Estimates

In this section, optical retrievals of the transverse horizontal wind are presented and compared with sonic measurements. Aggregate plots showing time series of the optically derived and sonic measured transverse horizontal wind velocity are plotted for the entire run starting from 2035 MDT on 15 June, 2010 and ending at 0545 MDT on 16 June, 2010. Individual scatter plots indicating the degree of agreement

between optically derived and sonic measured values of the transverse horizontal wind, for each of the five segments during this period are also shown. Numerical results are consolidated in the form of tables. Error statistics between the optically derived and sonic measured winds at different levels on the sonic towers and at two separate locations along the propagation path are also provided to quantify the performance of the two methods.

5.3.1 Optical Wind Estimates Using the Time-Delay-to-Peak Method

For the time-delay-to-peak method, AOA cross-correlation functions are computed for 10 s periods, over the entirety of each of the five segments. For each 10 s computation of the AOA cross-correlation function, the time delay to its peak, τ_p is calculated by parabolic curve fitting around the maxima followed by setting the slope of the curve to zero, as described in Section 4.3.1. One such instance of the AOA cross-correlation function and the τ_p calculation for a 10 s period beginning at 0403 MDT is as shown in Figure 5.6.
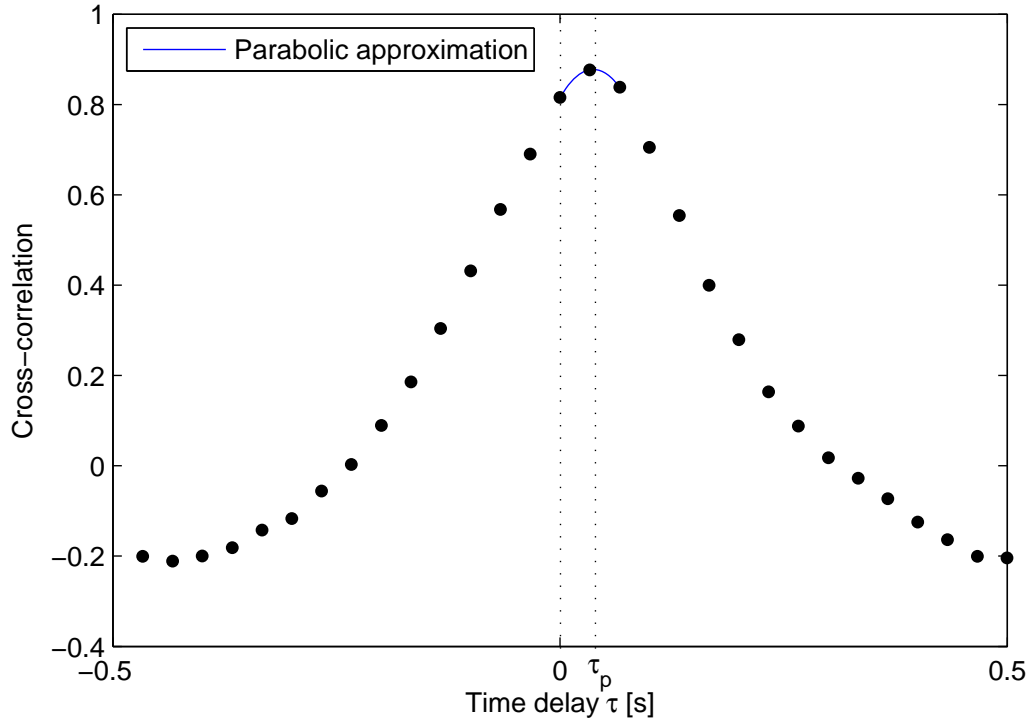
Figure 5.6. Extraction of τ_p from the AOA cross-correlation function. The solid blue line is the parabolic approximation for the AOA cross-correlation function around the maxima. The first derivative of this curve is set to zero to obtain the time delay to the peak τ_p.

Figure 5.7 shows a comparison between 10 s estimates of the wind retrieved optically by the time-delay-to-peak method and 10 s averages of the transverse horizontal wind measured by sonics at the level of the propagation path. Data from both towers is presented for all the five segments recorded. As noted previously, the optical propagation path crosses both the towers at ≈ 1.7 m AGL. This is approximately midway between sonic levels at 1.4 m and 2.1 m AGL on both towers. For the sake of simplicity, the transverse horizontal wind velocity at the level of the propagation path v_s as measured by the sonic is calculated by taking a simple average of the transverse horizontal wind velocities at 1.4 m and 2.1 m AGL for either tower. Once

v_s is obtained, it is used to calibrate for the proportionality constant γ_1 as described in Section 4.3.1. The optically estimated transverse horizontal wind velocity is then calculated using Equation 4.4.
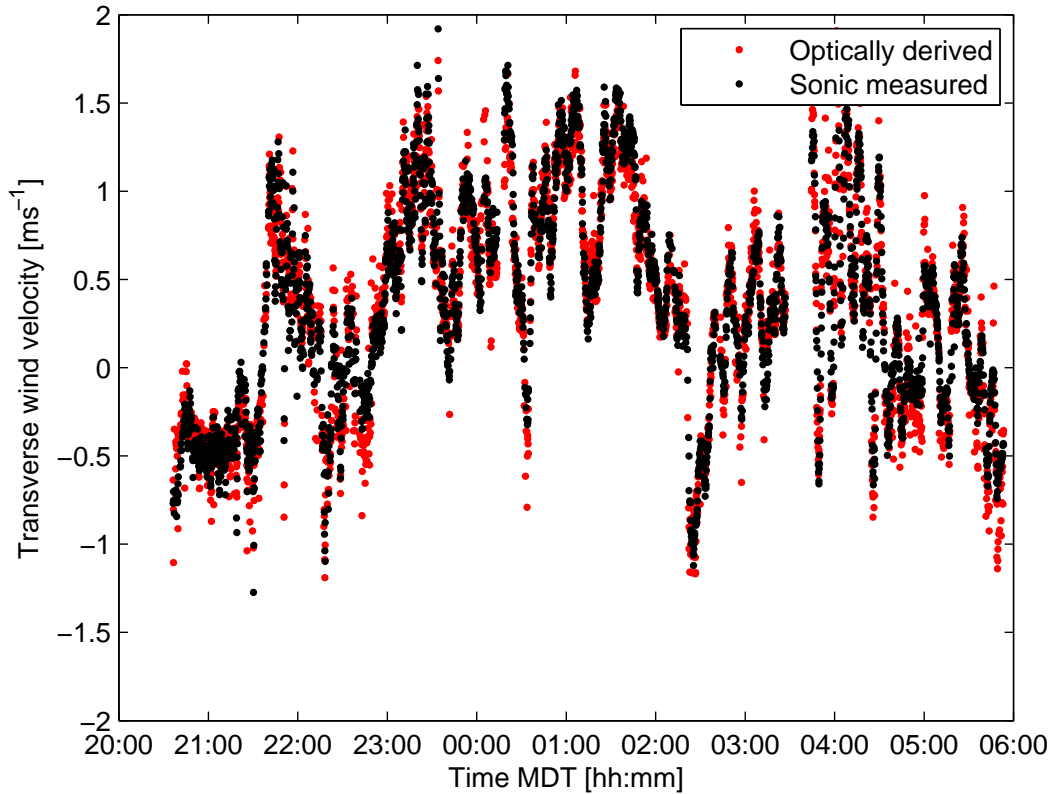
Figure 5.7. Optically derived and sonic measured velocity time series – time-delay-to-peak method (Tower 1). Red dots correspond to v_t – the velocity obtained by the time-delay-to-peak method, while the black dots correspond to v_s – the sonic measured velocity at $1.77\,\mathrm{m}$ AGL.

Illustrated in Figure 5.7 is the comparison between the two time series – the sonic measured and the optically estimated transverse horizontal wind velocity for Tower 1. The red dots correspond to the optically estimated values, while the black dots correspond to the sonic measured values of the transverse horizontal wind at $1.77\,\mathrm{m}$

AGL. As is seen, the optically estimated and sonic measured transverse horizontal wind velocities track each other very well throughout all the segments analyzed. This is also evident from the scatter plot shown in Figure 5.8.
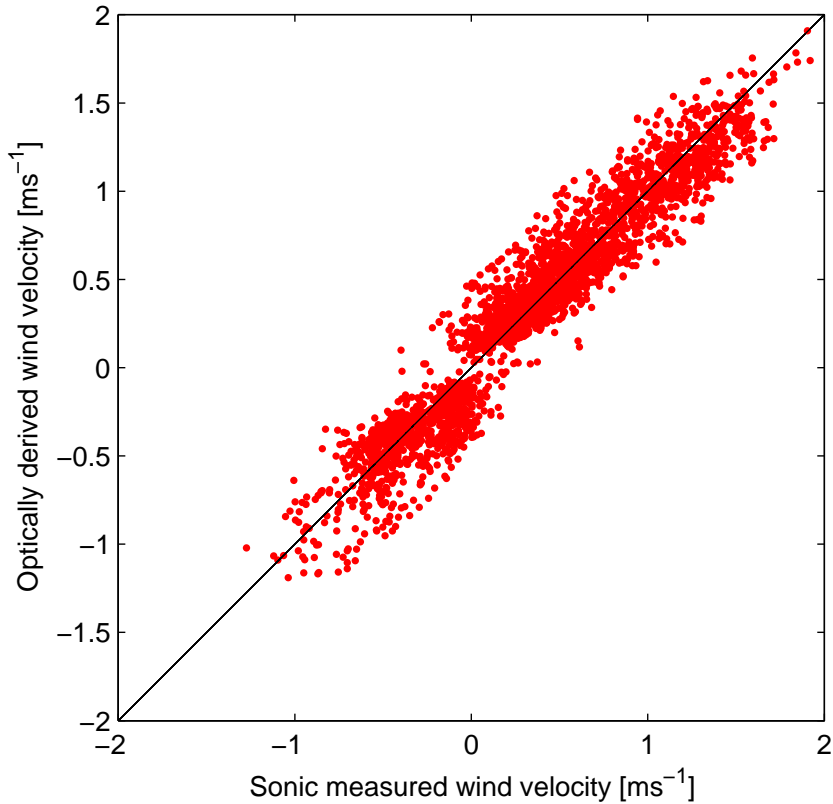
Figure 5.8. Scatter plot of optically derived (v_t) vs. sonic measured (v_s) velocities – time-delay-to-peak method (Tower 1). The narrow band around $0\,\mathrm{ms}^{-1}$ which is void of any v_t values can be attributed to the fact that the maximum range for the time delay τ is $\pm2\,\mathrm{s}$. This eliminates all velocity components which produce time delays to peaks outside this range of τ values.

Close examination of the scatter plot of optically derived vs. sonic measured wind velocities reveals the inability of the time-delay-to-peak method to measure very low transverse winds. This should come as no surprise, given the fact that this method

makes use of Taylor's frozen turbulence hypothesis [19] to extract the transverse horizontal wind from estimates of the time delay to the peak of the AOA cross-correlation function. Large time delays (which correspond to very low values of the transverse horizontal wind) invalidate the applicability of Taylor's frozen turbulence hypothesis. In order to avoid generating meaningless velocity estimates, a limit is placed on the maximum time lag between β_1 and β_2 as $\pm 2\,\text{s}$, for the cross-correlation computation. Hence, any velocity components which produce lags greater than $\pm 2\,\text{s}$ to the AOA cross-correlation peak are automatically discarded, which leads to the narrow band void of optically derived wind velocities near $0\,\text{ms}^{-1}$ as seen in Figure 5.8.

Some statistics of the velocity data shown in Figures 5.7 and 5.8 are listed in Table 5.1. Velocity statistics of both – the optically derived and sonic measured transverse horizontal wind velocity for all of the five segments recorded are presented. The four columns depict the optically estimated and three sonic measured velocities (in cms^{-1}). The rows represent three statistics of each – mean ($\bar{v}$), standard deviation (σ_v) and the RMS error (σ_{err}) with respect to the optically estimated wind velocity. All heights indicated are AGL.

Table 5.1. Velocity statistics for the time-delay-to-peak method – Tower 1

Tower 1 - Segment 1			
Statistic	v_t @ 1.77 m	v_s @ 1.45 m	v_s @ 1.77 m	v_s @ 2.13 m
$\bar{v}$	-9.8	-9.6	-10.3	-11.2
σ_v	49	43.6	48.6	55.3
σ_{err}	0	19.3	17.9	20.1
Tower 1 - Segment 2			
Statistic	v_t @ 1.77 m	v_s @ 1.45 m	v_s @ 1.77 m	v_s @ 2.13 m
$\bar{v}$	63.6	57.7	65.7	75.1
σ_v	46.2	40.6	44.7	50.2
σ_{err}	0	18.2	17.7	19.5
Tower 1 - Segment 3			
Statistic	v_t @ 1.77 m	v_s @ 1.45 m	v_s @ 1.77 m	v_s @ 2.13 m
$\bar{v}$	65.2	56.5	66.6	78.2
σ_v	62.8	60.1	65	71.7
σ_{err}	0	13.8	14.2	18.4
Tower 1 - Segment 4			
Statistic	v_t @ 1.77 m	v_s @ 1.45 m	v_s @ 1.77 m	v_s @ 2.13 m
$\bar{v}$	33	27.5	30.5	34.2
σ_v	28.4	26.4	26.2	27.4
σ_{err}	0	14.5	14.4	15.8
Tower 1 - Segment 5			
Statistic	v_t @ 1.77 m	v_s @ 1.45 m	v_s @ 1.77 m	v_s @ 2.13 m
$\bar{v}$	21.7	23	24.4	26.4
σ_v	58	49.8	53.5	59
σ_{err}	0	18.5	17.1	18.2

A similar analysis is carried out for sonic data from Tower 2, which was located a further 61 m north of Tower 1. The following Figure 5.9 shows the comparison between the two time series – the sonic measured and the optically estimated transverse horizontal wind velocity for Tower 2. The red dots correspond to the optically estimated values while the black dots correspond to the sonic measured values of the transverse horizontal wind at the level of the optical propagation path.
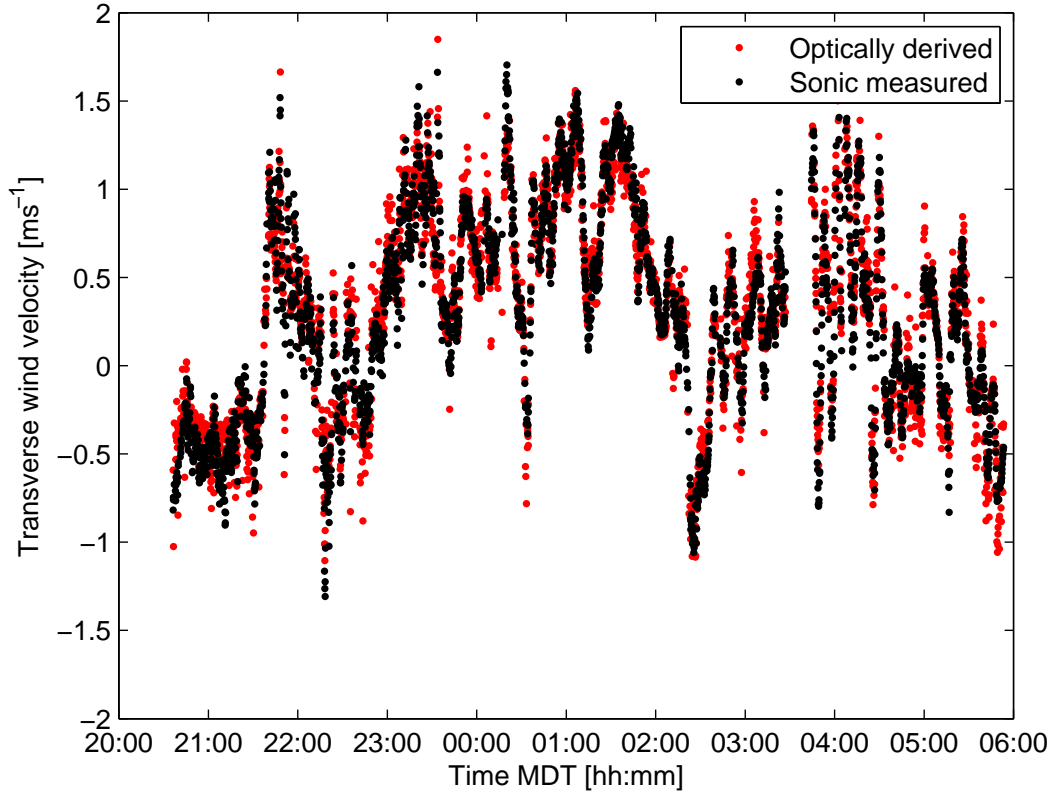
Figure 5.9. Optically derived and sonic measured velocity time series – time-delay-to-peak method (Tower 2). Red dots correspond to v_t – the velocity obtained by the time-delay-to-peak method, while the black dots correspond to v_s – the sonic measured velocity at 1.77 m AGL.

As is seen from the figure above, the optically estimated and sonic measured transverse horizontal wind velocities track each other very well throughout all the segments analyzed. This is also evident from the scatter plot shown in Figure 5.10. Similar to the scatter plot illustrated in Figure 5.8 for Tower 1 data, the scatter plot for Tower 2 exhibits a narrow band around $0\,\mathrm{ms}^{-1}$ which is void of optically derived values of the transverse horizontal wind. This, again arises from the constraint placed on the maximum time shift, τ, between β_1 and β_2, as $\pm 2\,\mathrm{s}$ for the cross-correlation computation.
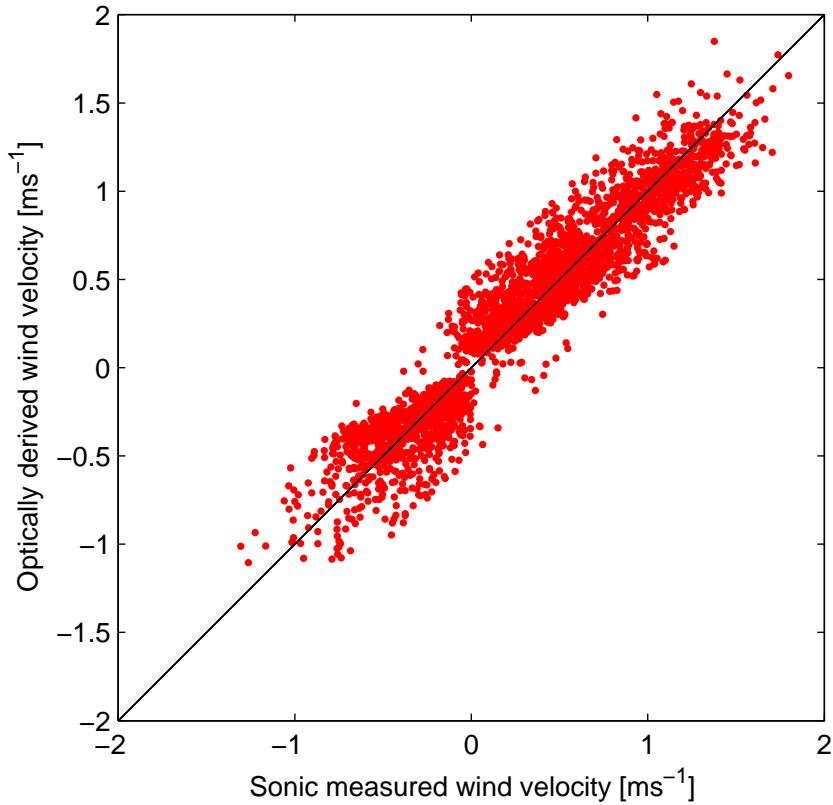
Figure 5.10. Scatter plot of optically derived (v_t) vs. sonic measured (v_s) velocities – time-delay-to-peak method (Tower 2). The narrow band around 0 which is void of any v_t values can be attributed to the fact that the maximum range for the time delay τ is ± 2 s. This eliminates all velocity components which produce time delays to peaks outside this range of τ values.

The results of the above analyses are summarized in Table 5.2. All velocities enlisted therein are estimated/measured using sonic data from Tower 2. Velocity statistics for optically derived and sonic measured transverse horizontal wind velocity are presented for each of the five segments recorded. The four columns depict the optically estimated and three sonic measured velocities (in cms^{-1}). The rows represent three statistics of each – mean $(\bar{v})$, standard deviation (σ_v) and the RMS error (σ_{err}) with respect to the optically estimated wind velocity. All heights indicated are AGL.

Table 5.2. Velocity statistics for the time-delay-to-peak method – Tower 2

Tower 2 - Segment 1			
Statistic	v_t @ 1.77 m	v_s @ 1.42 m	v_s @ 1.77 m	v_s @ 2.09 m
$\bar{v}$	-10.2	-12.7	-14	-15
σ_v	45.2	44.6	49.6	54.1
σ_{err}	0	19.5	19.4	21.3
Tower 2 - Segment 2			
Statistic	v_t @ 1.77 m	v_s @ 1.42 m	v_s @ 1.77 m	v_s @ 2.09 m
$\bar{v}$	57.8	47.5	58.3	67.7
σ_v	43.7	37.7	42.9	47.5
σ_{err}	0	18.7	18.6	20.4
Tower 2 - Segment 3			
Statistic	v_t @ 1.77 m	v_s @ 1.42 m	v_s @ 1.77 m	v_s @ 2.09 m
$\bar{v}$	60.6	48.4	60.9	72.1
σ_v	57.8	55.8	62	67.2
σ_{err}	0	13.8	15.1	18.9
Tower 2 - Segment 4			
Statistic	v_t @ 1.77 m	v_s @ 1.42 m	v_s @ 1.77 m	v_s @ 2.09 m
$\bar{v}$	30.3	20.6	27.7	34.1
σ_v	26.6	24.4	23.4	22.7
σ_{err}	0	17.1	16.3	16.6
Tower 2 - Segment 5			
Statistic	v_t @ 1.77 m	v_s @ 1.42 m	v_s @ 1.77 m	v_s @ 2.09 m
$\bar{v}$	17.7	11.7	16.5	20.8
σ_v	53.6	47.7	51.1	53.8
σ_{err}	0	18.5	17.2	18

5.3.2 Optical Wind Estimates Using the Slope-at-Zero-Lag Method

As with the time-delay-to-peak method, AOA cross-correlation functions are computed for 10 s periods over the entirety of each of the five segments recorded. For each 10 s computation of the AOA cross-correlation function, the slope at zero lag of the AOA cross-correlation function is calculated by fitting a polynomial of degree three around zero lag, followed by evaluating the slope of this polynomial at zero lag. The slope at zero lag is then normalized by the value of the AOA cross-correlation at zero lag. The details of the above computation are described in Section 4.3.2. One

such instance of the AOA cross-correlation function and its corresponding slope at zero lag for a 10 s period beginning at 0403 MDT is as shown in Figure 5.11.
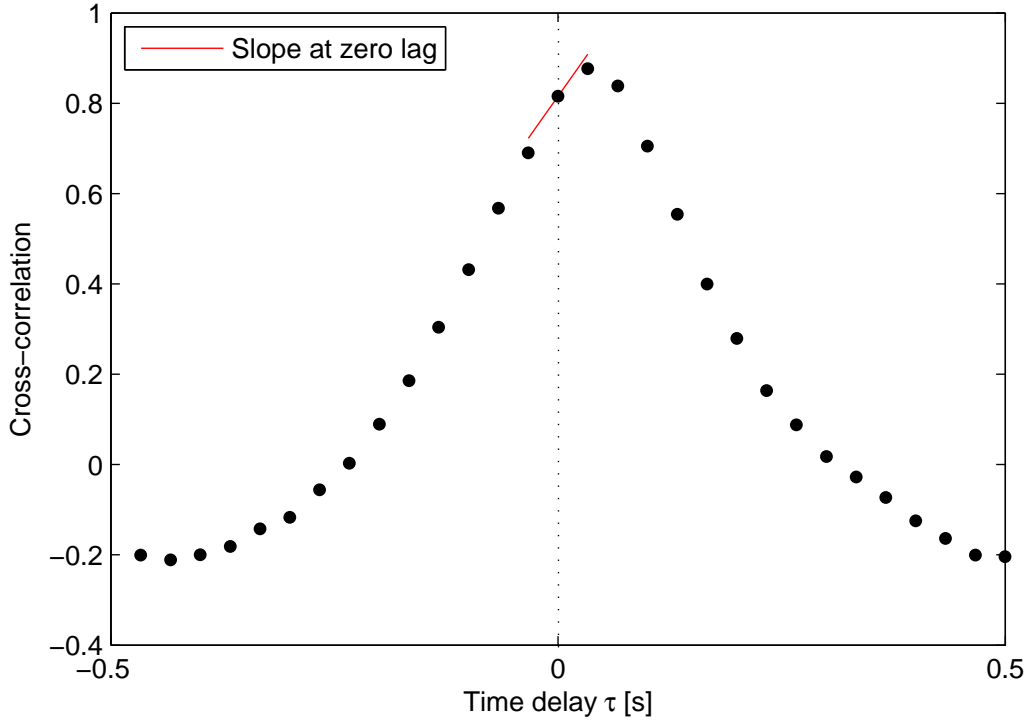
Figure 5.11. Extraction of the slope at zero lag of the AOA cross-correlation function. The solid red line is the tangent to the AOA cross-correlation function at zero lag. The slope of this line yields the slope at zero lag of the AOA cross-correlation function. It is obtained by evaluating at zero lag, the first derivative of a third degree polynomial that is fit to the AOA cross correlation function.

Optical wind retrievals using the slope-at-zero-lag method are presented below. Similar to the time-delay-to-peak method, optically derived velocities are compared with sonic measured values at the level of the optical propagation path. Sonic velocities are obtained by taking the average of the transverse horizontal wind at levels 1.4 m and 2.1 m AGL. Optical estimates of the transverse horizontal wind v_t are obtained using Equation 4.6, after the constant of proportionality γ_2 has been obtained

using the calibration procedure described in Section 4.3.2. Shown below is Figure 5.12 which depicts the time series of the sonic measured and optically estimated transverse horizontal wind velocity for Tower 1. The optically estimated values of the transverse horizontal wind have been obtained using Equation 4.6 and are represented by blue dots. The black dots correspond to the sonic measured value of the transverse horizontal wind at the level of the propagation path.

Figure 5.12. Optically derived and sonic measured velocity time series – slope-at-zero-lag method (Tower 1). Blue dots correspond to v_t – the velocity obtained by the slope-at-zero-lag method, while the black dots correspond to v_s – the sonic measured velocity at 1.77 m AGL.

Figure 5.13. Scatter plot of optically derived (v_t) vs. sonic measured (v_s) velocities – slope-at-zero-lag method (Tower 1). As opposed to the time-delay-to-peak method, the slope-at-zero-lag method is sensitive to velocities even closer to zero. This is because the slope-at-zero-lag method is immune to eddy decay caused by large time delays of propagation, which, as mentioned before, invalidates the applicability of Taylor's frozen turbulence hypothesis for the time-delay-to-peak method.

It is again observed that the sonic measured and optically estimated wind velocities track each other well throughout all of the five segments analyzed. The aggregate scatter plot for the five segments is shown in Figure 5.13. From the scatter plot shown above, it may be noted that there is no band around $0\,\mathrm{ms}^{-1}$ which is void of optically derived values of the transverse horizontal wind, unlike the time-delay-to-peak method. This is to be expected as the slope-at-zero-lag method does not rely on Taylor's frozen turbulence hypothesis for extracting the wind velocity. Instead, it relies

on the comparison of features of the cross-correlation between β_1 and β_2 around zero lag. Some of the velocity statistics for the data plotted in Figures 5.12 and 5.13 are listed in Table 5.3 below.

Table 5.3. Velocity statistics for the slope-at-zero-lag method – Tower 1

Tower 1 - Segment 1			
Statistic	v_t @ 1.77 m	v_s @ 1.45 m	v_s @ 1.77 m	v_s @ 2.13 m
$\bar{v}$	-8.5	-8.2	-9	-10
σ_v	43.5	41.3	45.9	52.2
σ_{err}	0	20.9	20.4	23
Tower 1 - Segment 2			
Statistic	v_t @ 1.77 m	v_s @ 1.45 m	v_s @ 1.77 m	v_s @ 2.13 m
$\bar{v}$	51	50.4	57.6	66.2
σ_v	44.2	39.7	44	49.6
σ_{err}	0	22	22.1	24.1
Tower 1 - Segment 3			
Statistic	v_t @ 1.77 m	v_s @ 1.45 m	v_s @ 1.77 m	v_s @ 2.13 m
$\bar{v}$	54.8	51.6	61.5	72.8
σ_v	60.3	58.6	63.5	70.3
σ_{err}	0	23.9	23.2	25.5
Tower 1 - Segment 4			
Statistic	v_t @ 1.77 m	v_s @ 1.45 m	v_s @ 1.77 m	v_s @ 2.13 m
$\bar{v}$	26.4	25.2	28.3	32.1
σ_v	25.1	26.9	26.8	28.1
σ_{err}	0	20.4	20.4	21
Tower 1 - Segment 5			
Statistic	v_t @ 1.77 m	v_s @ 1.45 m	v_s @ 1.77 m	v_s @ 2.13 m
$\bar{v}$	14.1	18.2	19.1	20.5
σ_v	43.4	46.5	49.9	54.9
σ_{err}	0	19.3	20	23.1

A similar analysis using the slope-at-zero-lag method is carried out for sonic data from Tower 2, which was located a further 61 m north of Tower 1. Illustrated in Figure 5.14, is the comparison between the two time series – the sonic measured and the optically estimated transverse horizontal wind velocity for Tower 2.
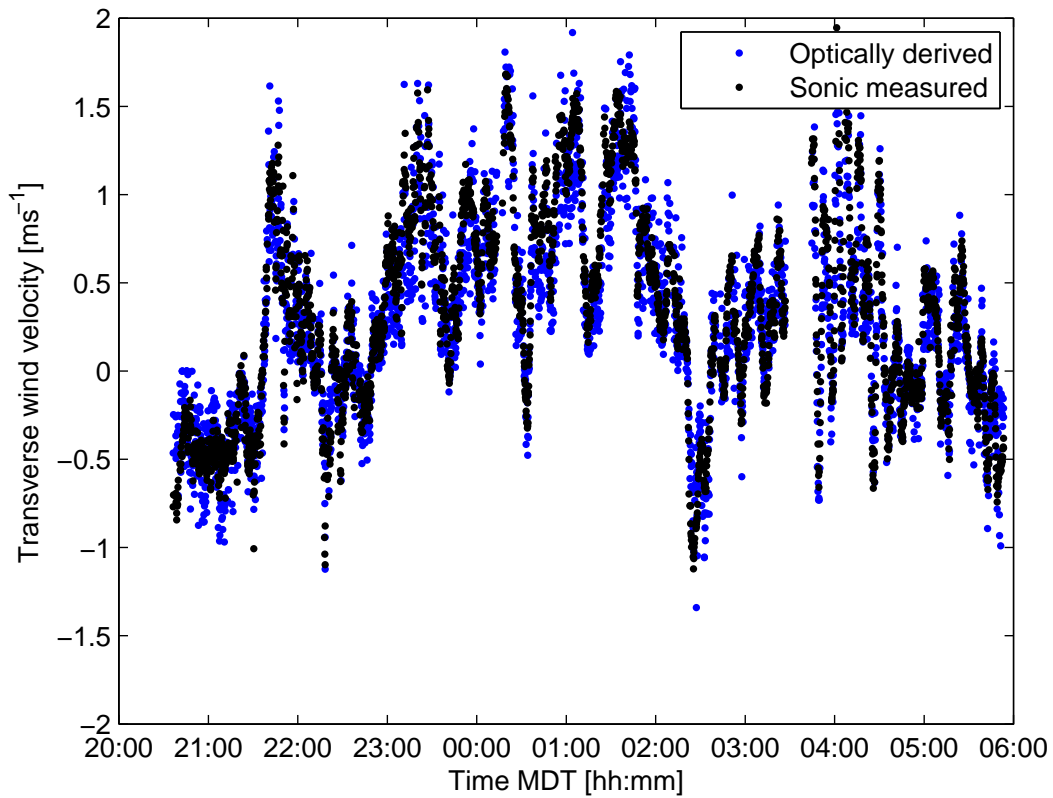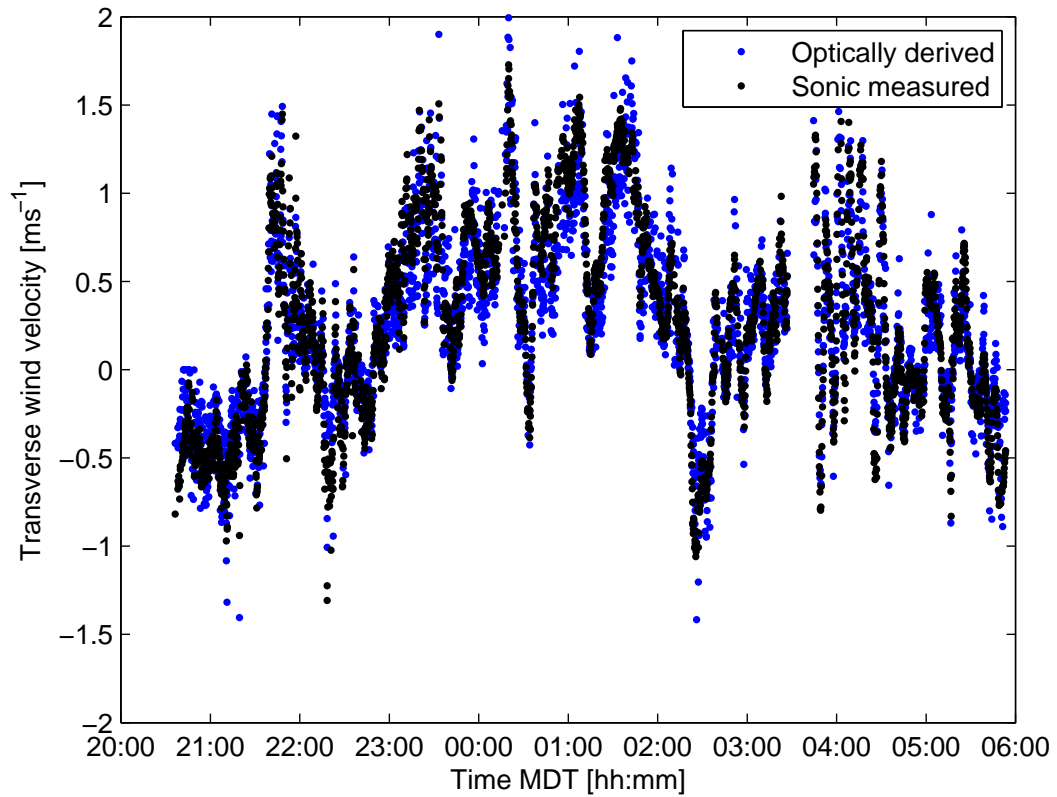
Figure 5.14. Optically derived and sonic measured velocity time series – slope-at-zero-lag method (Tower 2). Blue dots correspond to v_t – the velocity obtained by the slope-at-zero-lag method, while the black dots correspond to v_s – the sonic measured velocity at $1.77\,\mathrm{m}$ AGL.
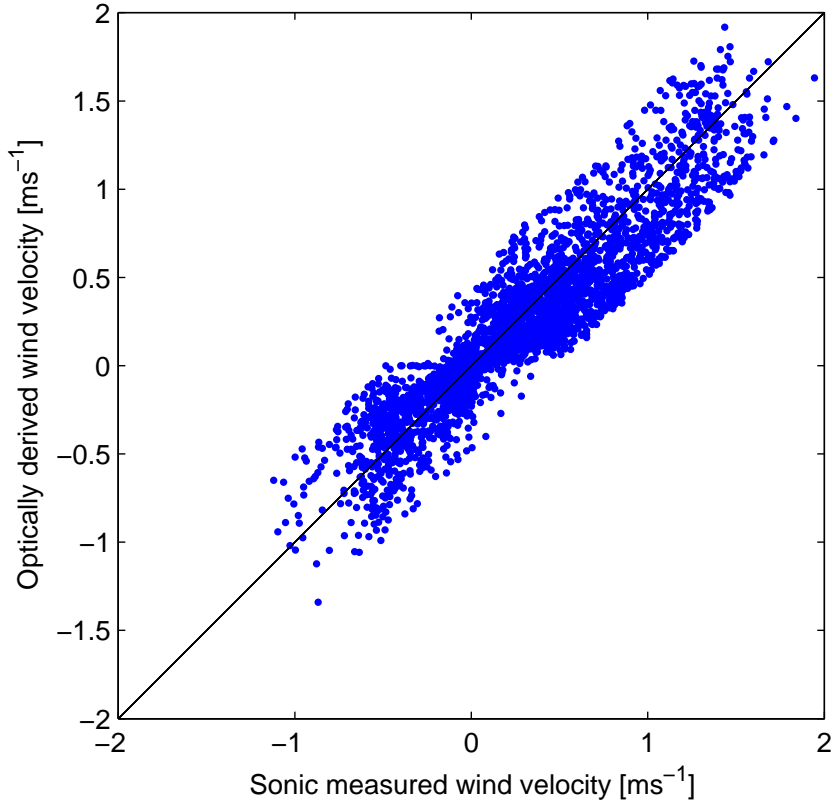
The aggregate scatter plot of optically derived versus sonic measured wind velocities (from Tower 2) for the five segments is shown in Figure 5.15.

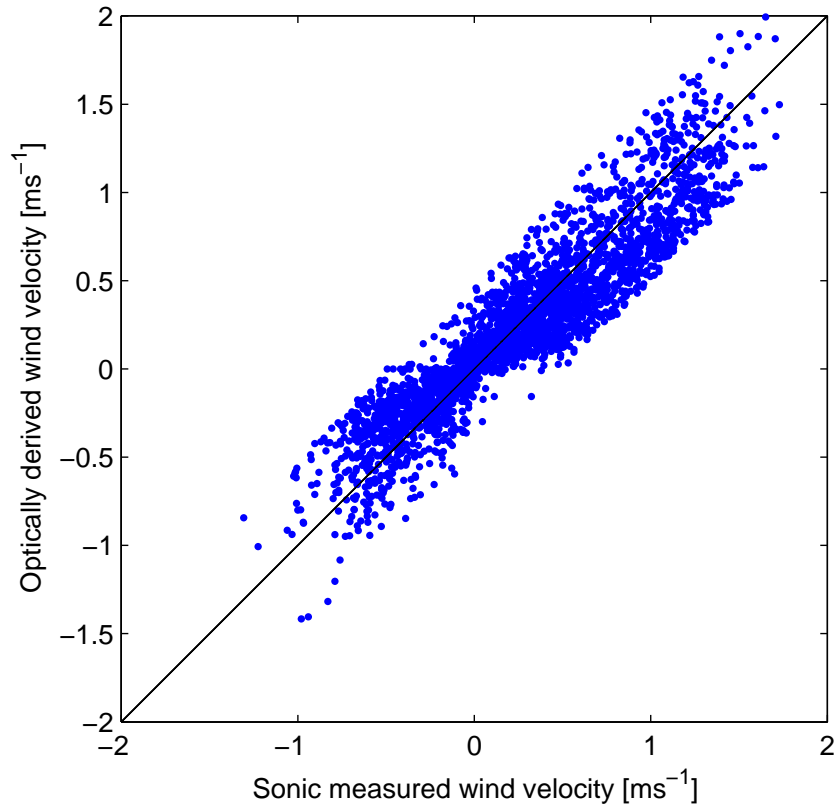**Figure 5.15.** Scatter plot of optically derived (v_t) vs. sonic measured (v_s) velocities – slope-at-zero-lag method (Tower 2). As opposed to the time-delay-to-peak method, the slope-at-zero-lag method is sensitive to velocities even closer to zero. This is because the slope-at-zero-lag method is immune to eddy decay caused by large time delays of propagation.

Table 5.4 lists some of the statistics for sonic measured and optically estimated wind velocities using the slope-at-zero-lag method.

Table 5.4. Velocity statistics for the slope-at-zero-lag method – Tower 2

Tower 2 - Segment 1			
Statistic	v_t @ 1.77 m	v_s @ 1.42 m	v_s @ 1.77 m	v_s @ 2.09 m
$\bar{v}$	−11.8	−10.8	−12.1	−13
σ_v	42.6	41.5	46.5	51
σ_{err}	0	19.5	19.4	21.2
Tower 2 - Segment 2			
Statistic	v_t @ 1.77 m	v_s @ 1.42 m	v_s @ 1.77 m	v_s @ 2.09 m
$\bar{v}$	47.9	43	52.8	61.4
σ_v	41.5	38	43.4	48.2
σ_{err}	0	21.1	21.4	23.3
Tower 2 - Segment 3			
Statistic	v_t @ 1.77 m	v_s @ 1.42 m	v_s @ 1.77 m	v_s @ 2.09 m
$\bar{v}$	49.9	43.9	56.1	67.1
σ_v	56	55.9	61.9	67
σ_{err}	0	23.8	24	25.8
Tower 2 - Segment 4			
Statistic	v_t @ 1.77 m	v_s @ 1.42 m	v_s @ 1.77 m	v_s @ 2.09 m
$\bar{v}$	24.4	18.1	25.3	31.9
σ_v	23.1	25.1	24.1	23.3
σ_{err}	0	17.9	17	17
Tower 2 - Segment 5			
Statistic	v_t @ 1.77 m	v_s @ 1.42 m	v_s @ 1.77 m	v_s @ 2.09 m
$\bar{v}$	13.3	8.7	13.2	17.5
σ_v	39.8	44.1	47.1	49.7
σ_{err}	0	19.2	19.4	20.8

CHAPTER 6

DISCUSSION

In this chapter, a qualitative analysis of the performance of the two optical wind retrieval methods is presented. First, a brief comparison of the two methods – the time-delay-to-peak and the slope-at-zero-lag method is presented with respect to their relative accuracies and their sensitivity to fluctuations of the transverse wind along the propagation path. Subsequently, the performance of both the wind estimators is analyzed in the presence of noise.

6.1 Time-Delay-to-Peak versus Slope-at-Zero-Lag Method

From the results presented in Sections 5.3.1 and 5.3.2, it is evident that both methods have their own advantages and shortcomings. Figures 5.7 and 5.9 show that the time-delay-to-peak method is insensitive to transverse wind velocities close to zero (which correspond to a larger time delays to the peak of the AOA cross-correlation function). This is a direct consequence of the invalidity of Taylor's frozen turbulence hypothesis for such cases. On the other hand from Figures 5.12 and 5.14 it is seen that the slope-at-zero-lag method is immune to large time delays. Because the slope-at-zero-lag method involves comparison of features close to zero lag, there is no risk of invalidating Taylor's frozen turbulence hypothesis. Hence, the slope-at-zero-lag method is ideal for measuring low values of the transverse wind.

Shown in Figure 6.1 is a scatter plot of the velocities obtained by the time-delay-to-peak versus the slope-at-zero-lag method for Tower 1.

49

Figure 6.1. Scatter plot of optically derived transverse wind velocities using the time-delay-to-peak and the slope-at-zero-lag method (Tower 1). As expected, the plot constricts around velocities near zero due to the inability of the time-delay-to-peak method to measure low wind velocities.

In Figure 6.1, a sharp constriction can be seen in the scatter plot around the velocities corresponding to $0\,\mathrm{ms}^{-1}$. Hence, it is evident that the time-delay-to-peak method suffers from the inability to measure low values (very close to zero) of the transverse wind. This stems from the previously mentioned shortcoming in the applicability of Taylor's frozen turbulence hypothesis, due to a large time delay to the peak of the AOA cross-correlation function. A similar behavior is observed for the scatter plot of the velocities obtained by the time-delay-to-peak versus the slope-at-zero-lag method for Tower 2, as illustrated in Figure 6.2.
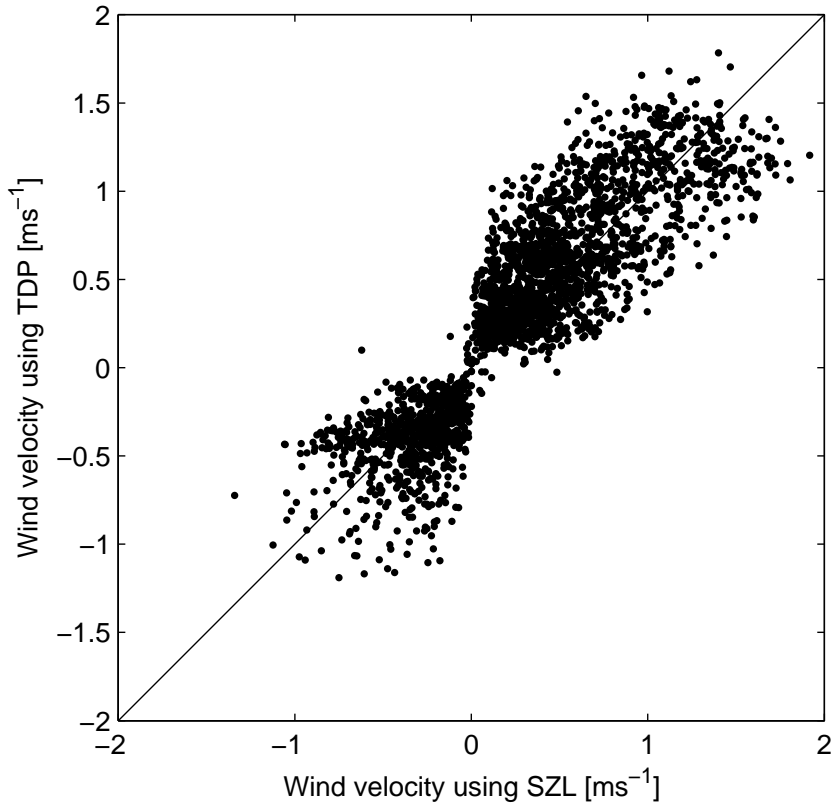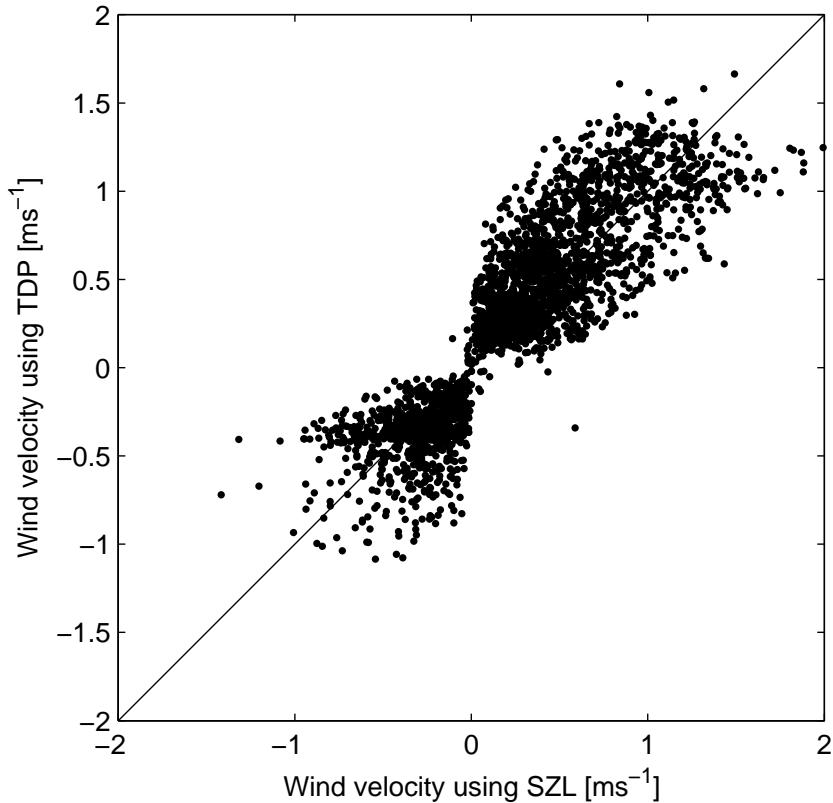
Figure 6.2. Scatter plot of optically derived transverse wind velocities using the time-delay-to-peak and the slope-at-zero-lag method (Tower 2). Similar to data from Tower 1, the plot constricts around velocities near zero due to the inability of the time-delay-to-peak method to measure low wind velocities.

As shall be seen later, the increased scatter corresponding to higher wind velocities, as observed in Figures 6.1 and 6.2, can be attributed to the fact that the time-delay-to-peak method over-estimates the wind velocity in case of a non-uniform wind blowing across the propagation path.

For both wind estimation methods discussed – the time-delay-to-peak and the slope-at-zero-lag, it is assumed that a constant wind blows transverse to the propagation path along its entire length. This, obviously is a simplistic assumption and does

not hold in practice. To evaluate the effect of inhomogeneity of the transverse wind across the propagation path, assume that the contour of the AOA cross-correlation function is an ellipse in the ρ–τ plane [20][3], i.e.,

$$B_{\beta_1\beta_2}(\rho,\tau) \equiv f[(\rho - \bar{v}\tau)^2 + \sigma_v^2\tau^2] \tag{6.1}$$

where ρ is the baseline for a two point interferometer, $\bar{v}$ is the average value of the transverse wind over the propagation path and σ_v is the standard deviation of the transverse wind velocity along the propagation path.

The time delay to the peak of the AOA cross-correlation function is obtained by setting $\partial B_{\beta_1\beta_2}/\partial\tau = 0$. Using Equation 6.1, the value of the time delay to the peak of the AOA cross-correlation function τ_p, is obtained as follows:

$$\frac{\partial B_{\beta_1\beta_2}(\rho,\tau)}{\partial\tau} = (2(\rho - \bar{v}\tau)(-\bar{v}) + 2\sigma_v^2\tau)\dot{f} \tag{6.2}$$

where the $\dot{}$ represents differentiation with respect to τ.

By setting the value of the derivative in Equation 6.2 as zero, the following is obtained:

$$2(\rho - \bar{v}\tau_p)(-\bar{v}) + 2\sigma_v^2\tau_p = 0$$

$$\Rightarrow (\rho - \bar{v}\tau_p)(\bar{v}) = \sigma_v^2\tau_p$$

$$\Rightarrow \rho\bar{v} - \bar{v}^2\tau_p = \sigma_v^2\tau_p$$

$$\Rightarrow \rho\bar{v} = \tau_p(\sigma_v^2 + \bar{v}^2)$$

$$\Rightarrow \tau_p = \frac{\rho\bar{v}}{(\bar{v}^2 + \sigma_v^2)} \tag{6.3}$$

The wind velocity, v_t, using Equations 4.4 and 6.3 can be obtained as follows:

$$v_t \sim \frac{\rho}{\tau_p} = \bar{v} + \frac{\sigma_v^2}{\bar{v}} \tag{6.4}$$

From Equation 6.4, it is evident that velocity estimates using the time-delay-to-peak method are contaminated by the inhomogeneity of the transverse wind along the propagation path. In other words a non-zero standard deviation of the transverse wind along the propagation path causes the time delay to the peak of the AOA cross-correlation function, τ_p to be estimated at value, lower than actual, thereby leading to an over estimation of the transverse wind velocity.

Similarly, the slope at zero lag of the AOA cross-correlation function is obtained by evaluating Equation 6.2 at $\tau = 0$ and is further normalized by the value of the AOA cross-correlation function at zero lag, which is obtained from Equation 6.1. This yields:

$$\left.\frac{\partial B_{\beta_1\beta_2}(\rho,\tau)}{\partial\tau}\right|_{\tau=0} = -2\rho\bar{v}\dot{f}(\rho^2)$$

$$\Rightarrow \frac{\left.\frac{\partial B_{\beta_1\beta_2}}{\partial\tau}\right|_{\tau=0}}{B_{\beta_1\beta_2}(\rho,0)} = \frac{-2\rho\bar{v}\dot{f}(\rho^2)}{B_{\beta_1\beta_2}(\rho,0)} \tag{6.5}$$

Using Equation 6.5 and Equation 4.6, the transverse wind velocity, v_t can be obtained as:

$$v_t \sim \bar{v} \tag{6.6}$$

Hence, it is seen from Equation 6.6 that the wind velocity estimates using the slope-at-zero-lag method are immune to variability of the transverse wind along the propagation path. Moreover, the time-delay-to-peak method over estimates the value of the transverse wind if there is a considerable non-zero wind variability along the propagation path. Given the above arguments, theoretically, it can be concluded that the slope-at-zero-lag method is a much more robust tool for the optical estimation of transverse wind velocity as compared to the time-delay-to-peak method.

6.2 Effect of Noise and Vibrations on Optical Wind Estimates

This section deals with the effects of addition of noise to the AOA signals, β_1 and β_2, on the performance of the two wind estimators – the time delay to the peak and the slope at zero lag of the AOA cross-correlation function. Two cases of noise are considered – white noise in the centroid estimates computed from the digital CCD-camera images and wind induced vibrations.

6.2.1 Noise in the CCD-camera Images

Consider the two AOA signals, β_1 and β_2 to be represented by Fourier-Stieltjes integrals (Chapter 1 in [18]).

$$
\begin{aligned}
\beta_1(t) &= \int_{-\infty}^{\infty} e^{j\omega t}\, dZ_1(\omega) \\
\beta_2(t) &= \int_{-\infty}^{\infty} e^{j\omega t}\, dZ_2(\omega)
\end{aligned}
\tag{6.7}
$$

where $dZ_1(\omega)$ and $dZ_2(\omega)$ are increments of random functions of ω. Similarly, white noise generated due to sampling/discretization at two separate locations on the CCD-camera photographic plate, can be represented by:

$$
\begin{aligned}
N_1(t) &= \int_{-\infty}^{\infty} e^{j\omega t}\, dN_1(\omega) \\
N_2(t) &= \int_{-\infty}^{\infty} e^{j\omega t}\, dN_2(\omega)
\end{aligned}
\tag{6.8}
$$

Adding these noisy signals to the AOAs represented by Equation 6.7:

$$
\begin{aligned}
\beta_{1N}(t) &= \int_{-\infty}^{\infty} e^{j\omega t}\, dZ_1(\omega) + \int_{-\infty}^{\infty} e^{j\omega t}\, dN_1(\omega) \\
\beta_{2N}(t) &= \int_{-\infty}^{\infty} e^{j\omega t}\, dZ_2(\omega) + \int_{-\infty}^{\infty} e^{j\omega t}\, dN_2(\omega)
\end{aligned}
\tag{6.9}
$$

Using the definition of the AOA cross-covariance function:

$$C_{\beta_{1N}\beta_{2N}}(\tau) = \langle \beta_{1N}^*(t)\beta_{2N}(t+\tau) \rangle \qquad (6.10)$$

Using the expressions from Equation 6.9 in Equation 6.10:

$$C_{\beta_{1N}\beta_{2N}}(\tau) = \left\langle \left(\int_{-\infty}^{\infty} e^{j\omega t}\, dZ_1(\omega) + \int_{-\infty}^{\infty} e^{j\omega t}\, dN_1(\omega) \right)^* \times \right.$$
$$\left. \left(\int_{-\infty}^{\infty} e^{j\omega'(t+\tau)}\, dZ_2(\omega') + \int_{-\infty}^{\infty} e^{j\omega'(t+\tau)}\, dN_2(\omega') \right) \right\rangle$$

Using $(A+B)^* = A^* + B^*$,

$$C_{\beta_{1N}\beta_{2N}}(\tau) = \left\langle \left(\int_{-\infty}^{\infty} e^{-j\omega t}\, dZ_1^*(\omega) + \int_{-\infty}^{\infty} e^{-j\omega t}\, dN_1^*(\omega) \right) \times \right.$$
$$\left. \left(\int_{-\infty}^{\infty} e^{j\omega'(t+\tau)}\, dZ_2(\omega') + \int_{-\infty}^{\infty} e^{j\omega'(t+\tau)}\, dN_2(\omega') \right) \right\rangle$$

$$\Rightarrow C_{\beta_{1N}\beta_{2N}}(\tau) = \left\langle \left(\int_{-\infty}^{\infty}\int_{-\infty}^{\infty} e^{j(\omega'-\omega)t} e^{j\omega'\tau}\, dZ_1^*(\omega)dZ_2(\omega') \right) + \right.$$
$$\left(\int_{-\infty}^{\infty}\int_{-\infty}^{\infty} e^{j(\omega'-\omega)t} e^{j\omega'\tau}\, dZ_1^*(\omega)dN_2(\omega') \right) + \left(\int_{-\infty}^{\infty}\int_{-\infty}^{\infty} e^{j(\omega'-\omega)t} e^{j\omega'\tau}\, dN_1^*(\omega)dZ_2(\omega') \right) +$$
$$\left. \left(\int_{-\infty}^{\infty}\int_{-\infty}^{\infty} e^{j(\omega'-\omega)t} e^{j\omega'\tau}\, dN_1^*(\omega)dN_2(\omega') \right) \right\rangle$$

$$\Rightarrow C_{\beta_{1N}\beta_{2N}}(\tau) = \int_{-\infty}^{\infty}\int_{-\infty}^{\infty} e^{j(\omega'-\omega)t} e^{j\omega'\tau} \langle dZ_1^*(\omega)dZ_2(\omega') \rangle +$$
$$\int_{-\infty}^{\infty}\int_{-\infty}^{\infty} e^{j(\omega'-\omega)t} e^{j\omega'\tau} \langle dZ_1^*(\omega)dN_2(\omega') \rangle + \int_{-\infty}^{\infty}\int_{-\infty}^{\infty} e^{j(\omega'-\omega)t} e^{j\omega'\tau} \langle dN_1^*(\omega)dZ_2(\omega') \rangle +$$
$$\int_{-\infty}^{\infty}\int_{-\infty}^{\infty} e^{j(\omega'-\omega)t} e^{j\omega'\tau} \langle dN_1^*(\omega)dN_2(\omega') \rangle$$

In the above expression, the cross-terms (terms with the ensemble average of AOA and noise) evaluate to zero as the AOA signals and noise are uncorrelated. Further,

55

because white noise added on to the AOAs at two different locations on the CCD-camera photographic plate is uncorrelated, the last term in the above expression also evaluates to zero. Thus, the above expression reduces to:

$$C_{\beta_{1N}\beta_{2N}}(\tau) = \int_{-\infty}^{\infty}\int_{-\infty}^{\infty} e^{j(\omega'-\omega)t}e^{j\omega'\tau} \langle dZ_1^*(\omega)dZ_2(\omega')\rangle \qquad (6.11)$$

Now, the following orthogonality relationship as described in Chapter 1 of [18], may be used:

$$\langle dZ_1^*(\omega)dZ_2(\omega')\rangle = W_{12}(\omega)\delta(\omega-\omega')\,d\omega d\omega' \qquad (6.12)$$

where $W_{12}(\omega)$ represents the two sided cross-spectrum of the AOAs, β_1 and β_2.

Using Equation 6.12 in Equation 6.11, the AOA cross-covariance is obtained as follows:

$$C_{\beta_{1N}\beta_{2N}}(\tau) = \int_{-\infty}^{\infty}\int_{-\infty}^{\infty} e^{j(\omega'-\omega)t}e^{j\omega'\tau}W_{12}(\omega)\delta(\omega-\omega')\,d\omega d\omega'$$

$$\Rightarrow C_{\beta_{1N}\beta_{2N}}(\tau) = \int_{-\infty}^{\infty} e^{j\omega\tau}W_{12}(\omega)\,d\omega \qquad (6.13)$$

Because the cross-covariance function and the cross-spectrum form a Fourier transform pair [18][7], the following is obtained by inversion of the right hand side of Equation 6.13:

$$C_{\beta_{1N}\beta_{2N}}(\tau) = C_{\beta_1\beta_2}(\tau) \qquad (6.14)$$

The above equation can be then modified to yield the AOA cross-correlation function as follows:

$$B_{\beta_{1N}\beta_{2N}}(\tau) = \frac{C_{\beta_1\beta_2}(\tau)}{\sqrt{(\sigma_{\beta_1}^2 + \sigma_{N_1}^2)(\sigma_{\beta_2}^2 + \sigma_{N_2}^2)}} \qquad (6.15)$$

where $\sigma_{\beta_i}^2$ and $\sigma_{N_i}^2; i = 1, 2$ represent the AOA and the noise variances, respectively.

Equation 6.15 for the AOA cross-correlation of noisy AOA signals can be expressed in terms of the AOA cross-correlation of clean AOA signals as shown below:

$$B_{\beta_{1N}\beta_{2N}}(\tau) = B_{\beta_1\beta_2}(\tau)\sqrt{\frac{\sigma_{\beta_1}^2\sigma_{\beta_2}^2}{(\sigma_{\beta_1}^2 + \sigma_{N_1}^2)(\sigma_{\beta_2}^2 + \sigma_{N_2}^2)}} \tag{6.16}$$

From Equation 6.16 it is evident that white noise from the CCD-camera, when added onto the AOA signals, β_1 and β_2, causes a loss in the correlation between them. This causes the noisy AOA cross-correlation function to be a scaled down version of the clean AOA cross-correlation function, while leaving the location of its peak, intact. Hence, white noise does not contaminate the estimates of the time delay to the peak of the AOA cross-correlation function. It may be observed though, that the scaling down of the AOA cross-correlation function as seen in Equation 6.16 can be corrected for. The term within the square-root sign of Equation 6.16 can be rewritten in terms of the Signal-to-Noise ratio, which if known beforehand, can be utilized to obtain the unbiased AOA cross-correlation function.

The slope-at-zero-lag wind estimate is calculated by evaluating the slope of the AOA cross-correlation function at $\tau = 0$ and then dividing it by the value of the AOA cross-correlation at $\tau = 0$. From Equation 6.15 it is seen that white noise causes the AOA cross-correlation function to scale down. This causes a decrease in the slope of the AOA cross-correlation function at zero lag. Hence, an underestimation of the wind velocity occurs due to the reduced slope of the AOA cross-correlation function at zero lag, when the AOA signals have been contaminated by incoherent white noise. Thus, it can be concluded that the time-delay-to-peak method is immune to incoherent white noise added on by the CCD-camera while the slope-at-zero-lag method is not (although this a minor drawback and the effect due to incoherent white noise can be easily corrected).

6.2.2 Wind-Induced Vibrations of the Telescope

Vibrations can be a major source of error, especially when the telescope body is impinged by sharp wind gusts. These wind induced vibrations can be thought of as sinusoidal signals with a random initial phase. Hence, they can be modeled as follows:

$$N(t) = A_N e^{j[\omega_N(t-t_0)]} \tag{6.17}$$

where A_N is the amplitude, ω_N is the frequency, t_0 is a random start time for the vibrations.

Utilizing Equations 6.7 and 6.17 the noisy AOA signals, β_1 and β_2 can be written as:

$$\begin{aligned}
\beta_1(t) &= \int_{-\infty}^{\infty} e^{j\omega t}\, dZ_1(\omega) + A_N e^{j[\omega_N(t-t_0)]} \\
\beta_2(t) &= \int_{-\infty}^{\infty} e^{j\omega t}\, dZ_2(\omega) + A_N e^{j[\omega_N(t-t_0)]}
\end{aligned} \tag{6.18}$$

Using the procedure described in Section 6.2.1 on Equation 6.18, the AOA cross-covariance function is obtained as:

$$\begin{aligned}
C_{\beta_{1N}\beta_{2N}}(\tau) = \int_{-\infty}^{\infty}\int_{-\infty}^{\infty} e^{j(\omega'-\omega)t}e^{j\omega'\tau}\, \langle dZ_1^*(\omega)dZ_2(\omega')\rangle + \\
A_N \int_{-\infty}^{\infty} e^{j(\omega_N-\omega)t}e^{j\omega_N\tau}\, \langle dZ_1^*(\omega)e^{-j\omega_N t_0}\rangle + A_N \int_{-\infty}^{\infty} e^{j(\omega'-\omega_N)t}e^{j\omega'\tau}\, \langle e^{j\omega_N t_0}dZ_2(\omega')\rangle + \\
A_N^2 e^{j\omega_N\tau} \quad (6.19)
\end{aligned}$$

Because the vibrations and the AOAs are uncorrelated, the ensemble averages of the cross-terms in Equation 6.19 go to zero. Again utilizing the orthogonality relationship listed in Equation 6.12, the expression for the AOA cross-covariance in the presence of coherent vibration noise becomes:

$$C_{\beta_{1N}\beta_{2N}}(\tau) = C_{\beta_1\beta_2}(\tau) + A_N^2 \cos(\omega_N\tau) \tag{6.20}$$

58

Hence, it is seen from Equation 6.20 that vibration noise contaminates the clean AOA cross-covariance function by adding a sinusoidal signal of frequency ω_N. This will lead to errors in both the time delay to the peak and the slope at zero lag of the AOA cross-correlation. Hence, vibration noise has much more drastic implications on the performance of these two wind estimators as compared to white noise. These observations are consistent with corresponding findings for the same two methods, made by the optical as well as the Spaced Antenna (SA) radar community [20][10][11][23].

CHAPTER 7

SUMMARY, CONCLUSIONS, AND OUTLOOK

In this chapter, a summary of the results and conclusions from the previous chapters is presented. Subsequently, some possibility for future work is discussed.

Results presented in Section 5.3, showing the comparison of optically estimated and in-situ measured values of the transverse horizontal wind, demonstrate the capability of optical AOAs for making remote wind measurements. Both, remote (optical) and in-situ (sonic) measurements of the transverse horizontal wind vector were carried out on a relatively calm night, starting on 15 June, 2010 for a period of approximately 9 h, during which the transverse horizontal wind varied between $-1\,\mathrm{m\,s^{-1}}$ and $2\,\mathrm{m\,s^{-1}}$. For this period, optical estimates ($10\,\mathrm{s}$ averages) of the transverse horizontal wind velocity using the time-delay-to-peak method had an RMS error (with respect to sonic measured values) no greater than $0.2\,\mathrm{m\,s^{-1}}$ for either tower. The same statistic for the optically estimated transverse horizontal wind velocity using the slope-at-zero-lag method was found not to exceed $0.24\,\mathrm{m\,s^{-1}}$ for either tower. These figures constitute only a small fraction (6–8%) of the peak-to-peak variation of the transverse horizontal wind velocity ($\approx 3\,\mathrm{m\,s^{-1}}$), and thus warrant the good accuracy of the two optical methods for remote wind measurements, presented in this thesis.

Although quite accurate, the two wind retrieval methods do suffer from inherent deficiencies. The invalidity of Taylor's frozen turbulence hypothesis at very low wind speeds causes the time-delay-to-peak method to be inapplicable. On the other

hand, the slope-at-zero-lag method suffers from an under estimation of high wind velocities due to reduction in the slope of the AOA cross-correlation function as its peak approaches zero lag. The slope-at-zero-lag method is immune to the random inhomogeneities of the transverse horizontal wind along the propagation path, while the time-delay-to-peak method yields over estimated transverse wind speeds in the presence of a non-zero wind variance along the propagation path. In terms of the noise performance, the time-delay-to-peak method is immune to white noise added on to the images of the light array by the CCD-camera. The same incoherent noise on the other hand, leads to a bias in the slope-at-zero-lag wind estimator due to a reduction in the AOA cross-correlation at zero lag. Both methods suffer equally badly in the presence of wind-induced, quasi-sinusoidal vibrations.

The optical wind estimates described in this thesis rely on a calibration process based on in-situ measured wind velocities. Thus, a natural course of action would be to obtain closed form expressions for the time delay to the peak and the slope at zero lag of the AOA cross-correlation function so that they may be directly used for optical wind estimation. This theoretical exercise would be along the lines of the work of Clifford [6], albeit within the framework of geometrical optics, so as to simplify the analysis; see [5]. A third method which can be potentially used for optical wind measurements is the slope-of-phase-spectrum method. The phase spectrum of the AOAs can be expected to be linear in frequency bands within which Taylor's frozen turbulence hypothesis is valid. Thus, the slope of the linear portion of the phase spectrum should also provide an estimator which is equivalent to the time delay to the peak of the AOA cross-correlation function. The use of the frequency domain for optical wind estimation has an added advantage of robustness to wind induced vibrations because such vibrations are usually narrow-band signals. The resonance frequencies at which such vibrations occur, are functions of the mechanical

characteristics of the telescope. These frequencies can be filtered out by a band-reject (or notch) filter, so as to obtain cleaner wind estimates. Other methods which may warrant further investigation within the context of optical wind estimation using AOAs, are the cross-correlation ratio (CCR) method and the intercept (INT) method described by Zhang *et al.* (2003) and Holloway *et al.* (1997), respectively [22][11].

BIBLIOGRAPHY

[1] Behn, M., Hohreiter, V., and Muschinski, A. A scalable data-logging system with serial interfaces and integrated GPS time-stamping. *J. Atmos. Oceanic Technol. 25* (2008), 1568–1578.

[2] Briggs, B. H. Radar observations of atmospheric winds and turbulence: a comparison of techniques. *J. Atmos. Terr. Phys. 42* (1980), 823–833.

[3] Briggs, B. H., Phillips, G. J., and Shinn, D. H. The analysis of observations on spaced receivers on the fading of radio signals. *Proc. Phys. Soc. London 63* (1950), 106–121.

[4] Briggs, B. H., and Spencer, M. Horizontal movements in the Ionosphere. *Reports On Progress In Physics 17* (1954), 245–280.

[5] Cheon, Y., Hohreiter, V., Behn, M., and Muschinski, A. Angle-of-arrival anemometry by means of a large-aperture Schmidt-Cassegrain telescope equipped with a CCD camera. *J. Opt. Soc. Am. A 24* (2007), 3478–3492.

[6] Clifford, S. F. Temporal-frequency spectra for a spherical wave propagating through atmospheric turbulence. *J. Opt. Soc. Am. 61* (1971), 1285–1292.

[7] Clifford, S. F. The classical theory of wave propagation in a turbulent medium. In *Laser beam propagation in the atmosphere*, J. W. Strohbehn, Ed. Springer, Berlin, 1978, pp. 9–43.

[8] Clifford, S. F., Ochs, G. R., and Wang, T. I. Optical wind sensing by observing scintillations of a random scene. *Applied Optics 14*, 12 (1975), 2844–2850.

[9] Cohen, M. H., Gunderma, E. J., Hardebec, H. E., and Sharp, L. E. Interplanetary scintillations. 2. Observations. *Astrophysical Journal 147*, 2 (1967), 449–&.

[10] Doviak, R. J., Zhang, G. F., Cohn, S. A., and Brown, W. O. J. Comparison of spaced-antenna baseline wind estimators: Theoretical and simulated results. *Radio Sci. 39* (2004).

[11] Holloway, C. L., Doviak, R. J., Cohn, S. A., Lataitis, R. J., and Van Baelen, J. Cross correlation and cross spectra for spaced antenna wind profilers. 2. Algorithms to estimate wind and turbulence. *Radio Sci. 32* (1997), 967–982.

[12] Ishimaru, A. The beam wave case and remote sensing. In *Laser Beam Propagation in the Atmosphere*, J. W. Strohbehn, Ed., vol. 25 of *Topics in Applied Physics*. Springer, Berlin, Germany, 1978, pp. 129–170.

[13] Lataitis, R. J., Clifford, S. F., and Holloway, C. L. An alternative method for inferring winds from spaced-antenna radar measurements. *Radio Sci. 30* (1995), 463–474.

[14] Lawrence, R. S., Ochs, G. R., and Clifford, S. F. Use of scintillations to measure average wind across a light beam. *Appl. Opt. 11*, 2 (1972), 239–243.

[15] Lenschow, D. H. *Probing the Atmospheric Boundary Layer.* American Meteorological Society Press, Boston, 1986.

[16] Mitra, S. N. A radio method of measuring winds in the ionosphere. *Proceedings of the Institution of Electrical Engineers-London 96*, 43 (1949), 441–446.

[17] Rytov, S. M., Kravtsov, Y. A., and Tatarskii, V. I. *Principles of statistical radio physics – 4. Wave propagation through random media.* Springer, Berlin, Germany, 1989.

[18] Tatarskii, V. I. *The effects of the turbulent atmosphere on wave propagation.* Israel Program for Scientific Translation, Jerusalem, Israel, 1971.

[19] Taylor, G. I. The spectrum of turbulence. *Proc. Roy. Soc. A 164* (1938), 476–490.

[20] Wang, T. I., Ochs, G. R., and Lawrence, R. S. Wind measurements by the temporal cross-correlation of the optical scintillations. *Applied Optics 20* (1981), 4073–4081.

[21] Wheelon, A. D. *Electromagnetic scintillation — I. Geometrical optics.* Cambridge University Press, Cambridge, United Kingdom, 2001.

[22] Zhang, G. F., Doviak, R. J., Vivekanandan, J., Brown, W. O. J., and Cohn, S. A. Cross-correlation ratio method to estimate cross-beam wind and comparison with a full correlation analysis. *Radio Sci. 38* (2003).

[23] Zhang, G. F., Doviak, R. J., Vivekanandan, J., Brown, W. O. J., and Cohn, S. A. Performance of correlation estimators for spaced-antenna wind measurement in the presence of noise. *Radio Sci. 39* (2004).